Master's thesis

Optical performance of a Prototype Detector and Preliminary Design Studies for Large-Scale Ocean-based Neutrino Detector

(試作検出器の光学性能と大規模海洋ニュートリノ検出に向けた予備設計の研究)

Simran Chauhan

Department of Physics
Graduate school of Science
Tohoku University

2025

Abstract

Neutrinos are elusive particles that have challenged and enriched our understanding of particle physics since their discovery. Their ability to pass through matter makes them powerful probes for studying otherwise inaccessible regions like the Sun and the Earth's interior.

Spectroscopy of the Earth with anti neutrinos has opened up an exciting new field of neutrino geophysics, combining geochemistry and particle physics to study the Earth's chemical composition and internal heat production. Earth releases approximately 47×10^{12} joules of energy per second through primordial cooling and radioactive decay of long-lived isotopes. The exact contribution from each process remains uncertain. This internal heat drives mantle convection, powers plate tectonics, and sustains the geodynamo that generates Earth's magnetic field - essentially keeping the planet alive from within. Geoscientific models predict radiogenic heat contributions between 11 and 33 TW. Measuring the geoneutrino flux helps constrain and validate these models. Moreover, determining the absolute abundances of uranium and thorium helps estimate the abundances of 34 other refractory elements, offering insights into the Earth's composition through an entirely independent method.

The first groundbreaking detection of geoneutrinos was reported in 2005 by the KamLAND experiment in Gifu, Japan, followed by the Borexino experiment in Gran Sasso, Italy. Their results suggest a radiogenic heat production between 11 and 20 terawatts. However, the estimates carry significant uncertainties due to their locations on continental crust, which is enriched in heat-producing elements (HPEs). Because geoneutrino flux decreases with distance as an inverse square law, most of the detected signal originates from the local crust - whose composition is not accurately modeled, limiting the detectors' ability to identify geoneutrinos from deeper layers of the Earth. Isolating mantle contribution to geoneutrino flux is necessary to validate existing geoscientific models of radiogenic heat production of the Earth.

Started in 2019, a collaboration between Tohoku University and JAMSTEC aims to deploy a neutrino detector in the ocean off coast of Hawaii to detect geoneutrinos from mantle. This site, with thin oceanic crust and low radioactivity, enhances sensitivity to mantle geoneutrinos.

Currently a small prototype liquid scintillator detector is being developed to test its performance under deep-sea environment. This study presents the optical performance evaluation of the prototype detector in sea settings using Geant4 optical simulations. The impact of environmental and intrinsic backgrounds - including U, Th, K, and Co-60 in seawater, sediments, and detector components was quantified and found to be minimal. A preliminary design study of large scale detector was carried out to analyze the effect of thicknesses of detector components on the transmission efficiency of light.

Acknowledgment

I would like to express my sincere gratitude to my advisor, Associate Professor Hiroko Watanabe, for her continued mentorship, immense patience, and unwavering support throughout my master's program. I am also thankful to Professor Yasuhiro Kishimoto for his valuable suggestions to my thesis work, even though I consulted him relatively late in the process. My heartfelt thanks go to Professor Kunio Inoue for giving me the exciting opportunity to be a part of RCNS and the KamLAND project. I also thank Professor William McDonough for introducing me to the fascinating field of neutrino geoscience and rocks.

I would also like to thank my friends in the OBD group, Xu and Ono-kun, as well as former members Araki-san and Ohno-san; it was a pleasure and a valuable experience working with you all. I am deeply grateful to all my friends and seniors and teachers at RCNS for their kindness and warm welcome.

Finally, I would like to mention my family and friends back home whose constant support and encouragement helped me through challenging times. Without them, this journey would have been far more difficult and far less meaningful.

Contents

List of Figures

List of Tables

Chapter 1

Introduction and thesis overview

1.1 Scientific Motivation

Neutrinos are elusive elementary particles that offer unique opportunities for probing environments inaccessible by conventional observational methods. Geoneutrinos - electron antineutrinos produced by the radioactive decay of long-lived isotopes within Earth represent a novel tool to understand Earth's internal structure and radiogenic heat production. Measurements made by large liquid scintillator detectors, such as KamLAND and Borexino, have advanced the field significantly; however, their continental locations limit sensitivity to geoneutrinos originating from Earth's mantle.

Ocean-based neutrino detectors positioned on the ocean floor promise enhanced sensitivity to mantle geoneutrinos due to thinner oceanic crust and lower crustal radioactivity. The Ocean Bottom Detector (OBD) project, a collaborative effort between Tohoku University and JAMSTEC, aims to realize this potential by developing neutrino detectors deployable at great ocean depths. As a first step towards the realization of Ocean Bottom Detector, a deep sea prototype liquid scintillator detector is being developed whose primary objective is to demonstrate technological developments and long term stable performance of a liquid scintillator detector in deep sea environment.

1.2 Aim and objectives

Aim

To evaluate the optical performance of a deep-sea prototype liquid scintillator detector and conduct preliminary design studies for a large-scale ocean-based neutrino detector using Geant4 simulations.

Objectives

1. **Response and Optical Performance Evaluation via Simulation and Validation**: Simulate optical photon transport and photoelectron response for the prototype detector, validate the simulation result with an experimental setup. Simulate the detector configuration in the sea with improved light yield and find the intrinsic resolution of the detector.
2. **Modeling Environmental and Intrinsic Backgrounds**: Quantify the radiation backgrounds from seawater, sediments (U-238, Th-232, K-40), and construction materials (steel, acrylic, glass) by modeling their contributions using Geant4. Establish that such backgrounds do not significantly interfere with typical calibration sources like Cs-137.
3. **Preliminary Design Studies for a Large-Scale Ocean Bottom Detector**: Conduct ray-tracing studies for photon transmission in a multi-layered geometry of liquid scintillator–acrylic container–buffer oil layer for a large scale ocean based detector. Analyze how varying the thicknesses of the mediums affect light transmission.

1.3 Scope and Limitations

This work focuses specifically on predictive simulation studies performed using the Geant4 simulation toolkit. These studies aim to establish baseline expectations for prototype detector performance and stability under marine conditions. The prototype detector itself has not yet been deployed in the marine environment.

The detector response modeled here is limited to photoelectron distributions, representing an idealized optical output and resolution. Actual data after deployment, measured electronically, will require further calibration against these simulations, introducing systematic uncertainties.

For the large scale design studies, the results show better transmission efficiency in thinner acrylic and buffer oil medium but additional optimization involving mechanical constraints such as stress tolerance, pressure loading and radioactive impurity is needed to finalize these design parameters.

1.4 Thesis Outline

Following this introductory chapter, the thesis is structured as follows:

The next 3 chapters deal with the ultimate research background of the thesis.

Chapter 2 provides an overview of neutrino physics and has a detailed explanation of neutrino oscillations which are important to understand the survival probability of geoneutrinos reaching the detectors from interiors of the Earth in chapter 3.

Chapter 3 provides an extensive discussion on geoneutrinos and the insights they offer regarding the Earth's innermost regions. Additionally, it outlines the necessity of isolating geoneutrino signals originating from the mantle.

Chapter 4 describes the proposed design and strengths of an ocean based large sized neutrino detector to directly measure mantle geoneutrinos

From chapter 5 we start discussing about the development and simulation studies of a small prototype detector.

Chapter 5 explains the prototype detector design, detailing its components specifically chosen to withstand high-pressure marine conditions.

Chapter 6 focuses on the response of the prototype detector to external radiation especially a gamma calibration source and optical simulations to track the scintillation light to evaluate intrinsic resolution of detector.

Chapter 7 deals with the potential background that the detector could observe in the marine environment. It establishes a baseline model for predicting the energy response of the detector.

Chapter 8 addresses the large scale detector design preliminary study based on light transmission through various layers of the geometry of the detector.

Chapter 9 summarizes the thesis work in a conclusion and points the future prospects of this project.

Chapter 2

Neutrino Physics

2.1 The Standard Model

The Standard Model of particle physics is the foundation for understanding the smallest blocks of matter. It explains how three of the four fundamental forces (electromagnetic, weak, and strong) excluding gravitational force work and lists all currently known elementary particles. Fig 2.1 shows all these particles along with their mass, electric charge and spin. Other properties like hypercharge, isospin and color are not shown in the figure but can be deduced from the given information except color. All the

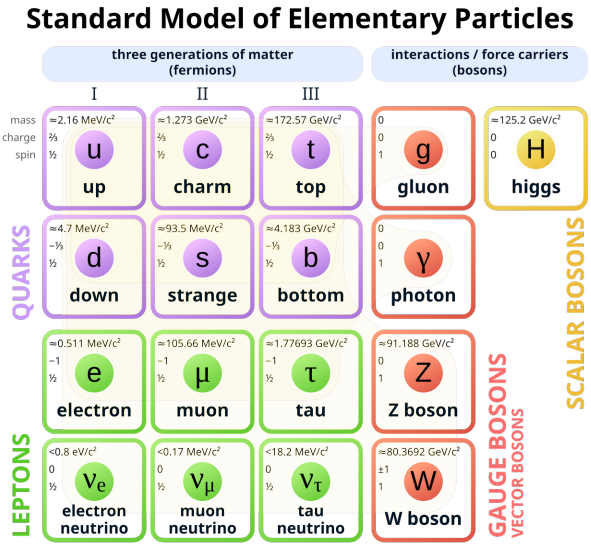

Figure 2.1: Elementary particles of Particle Physics in Standard Model

elementary matter particles are called fermions and are shown in the first three columns, while force carrier particles called bosons are shown in the fourth and fifth column. Fermions are sub-categorized into quarks and leptons. There are six kinds of quarks (up, down, charm, strange, top, and bottom) each with three different colors quantum numbers (not shown here) and six kinds of leptons (electron, muon, tau, electron neutrino, muon neutrino, tau neutrino).

Bosons are of two broader spin-dependent categories: gauge bosons (spin one) and scalar bosons (spin zero). There are four different kinds of gauge bosons (gluons, photon, Z boson, and W bosons) and one scalar boson (Higgs boson). Gluons are the carriers of strong forces, photons of electromagnetic forces, and W and Z boson of weak forces. Higgs boson is responsible for the masses of all the other particles except for neutrinos.

Faint brown loops in the background indicate which bosons couple to which fermions. Quarks couple to all gauge bosons, indicating they interact via all three forces. Electrons, muons, and taus couple

to photons, and W and Z bosons, indicating they interact via em and weak forces. Neutrinos, being electrically charge less, only couple to W and Z bosons, indicating they interact only via weak forces.

2.2 Discovery of neutrinos

The discovery of neutrinos is a landmark in the history of particle physics. In 1930, Wolfgang Pauli first proposed the existence of an unseen neutral particle to explain the apparent violation of energy and momentum conservation in beta decay. He suggested that this particle carried away the missing energy, but was extremely difficult to detect. In 1934, Enrico Fermi developed a theory of beta decay incorporating this particle, which he named the "neutrino" (meaning "little neutral one"). However, due to its lack of electric charge and tiny interaction cross-section, the neutrino remained hypothetical for decades. It wasn't until 1956 that Clyde Cowan and Frederick Reines experimentally confirmed the neutrino's existence by detecting antineutrinos emitted from a nuclear reactor in the famous Cowan-Reines experiment. This discovery not only validated Pauli's bold proposal but also opened a new frontier in understanding fundamental particles and forces and marking the start of experimental neutrino physics [1].

2.3 Sources of neutrinos

Neutrinos are the most abundant particles in the universe after photons. For every nucleon there are about a billion neutrinos in the universe. They are made in many places: inside stars, in nuclear reactors, deep inside Earth, and in space. They can travel huge distances even right through planets without being stopped. By figuring out where neutrinos come from, we can learn both about the neutrinos themselves and about the extreme places that create them.

We can broadly classify the sources like this:

Solar Proton–proton fusion in the Sun's core emits electron-neutrinos up to 20 MeV; roughly $6\times10^{10}/cm^2$ reach Earth every second. Because they exit the core unimpeded, they let us probe stellar fusion and flavor change in real time.

Astrophysical Supernovae release brief MeV bursts that carry away most of a collapsing star's energy, while TeV-PeV neutrinos from active galactic nuclei or gamma-ray bursts trace hadronic processes in extreme cosmic accelerators, traveling across the universe with minimal attenuation.

Reactor Fission fragments in nuclear reactors β decay, producing intense, controllable $\bar{\nu}_e$ beams below 10 MeV. Their well-known flux and adjustable baselines make precision oscillation studies possible, sterile-neutrino searches, and real-time reactor monitoring.

Geoneutrino β decays of U-238, Th-232, and K-40 in Earth's mantle and crust generate 1-3 MeV energy $\bar{\nu}_e$s. Detecting them constrains the planet's radiogenic heat output and tests compositional models beyond the reach of drilling or seismology.

Others Cosmic-ray air showers create atmospheric ν_μ and ν_e across 100 MeV to 100 GeV, while accelerator beams replicate part of this spectrum for long-baseline experiments that probe mass ordering and CP violation. Additionally, yet-undetected contributions may arise from relic Big-Bang neutrinos, dark-matter annihilation, or neutron-star mergers.

2.4 Interactions

Neutrinos are heavily abundant particles, but they are very hard to detect due to their low mass and no charge. Area of cross section of a neutrino interaction is very small, and is given by:

$$\sigma \sim G_F EM \sim 10^{-38} cm^2 \frac{EM}{GeV^2} \tag{2.1}$$

Here, G_F = Fermi constant, E = neutrino energy, M = mass of target particle.

The mean free path (λ) of a neutrino in a medium with number density N of target particles is given by:

$$\lambda \sim \frac{1}{N\sigma} \sim \frac{10^{38} cm^{-2}}{(Ncm^3)(EM/GeV^2)} \tag{2.2}$$

A 1MeV neutrino will have a cross section of about $10^{-41} cm^2$ with the target particle being nucleons of mass M $\sim$ 1 GeV. This corresponds to a mean free path of 10^{17} cm for normal matter with $N \sim N_A/cm^3 \sim 10^{24}/cm^3$, which is about 0.1 light years. Therefore, the chances of detecting a 1 MeV neutrino passing through Earth are very low. Such low probabilities of detection require huge detectors with a large number of target particles. Most neutrino detectors are located underground to shield them from cosmic rays and other background radiation.

Neutrinos only participate in weak interactions which are of two types:

Neutral current: In a neutral current (NC) interaction, only momentum and energy from a neutrino are passed to a target particle, and an exchange of Z boson is involved. All 3 flavors of neutrinos can engage in NC interactions. When the target particle has some charge and is sufficiently light, it can accelerate to relativistic speeds and emit Cherenkov radiation that can be detected directly. However, flavor of the interacting neutrino can't be determined through these processes.

Charged current: In a charged current (NC) interaction, a neutrino of sufficient energy interacts to produce its corresponding lepton. Here, we can determine the flavor of the neutrino that interacted from the knowledge of the lepton that is produced. A W boson is mediated in these interactions.

2.5 Neutrino Oscillations

In the Standard Model framework, neutrinos have 0 mass, but the discovery of neutrino oscillations proved otherwise.

The three types of neutrinos : electron ν_e , muon ν_μ, and tau ν_τ are not fixed but are superpositions of three mass eigenstates (ν_1, ν_2, ν_3). As neutrinos travel, the mass components shift phase at different rates, causing the overall flavor to change over time. It is an important property of neutrinos that makes them all the more elusive.

The problem started with observations of solar neutrinos by David et al. in 1968. They observed a significantly fewer number of solar neutrinos than what was theoretically predicted from the Standard Solar Model. In 1969, Pontecorvo and Gribov proposed an explanation for this problem - neutrinos oscillate from one flavor to another. Subsequently, in 1989, the Super-Kamiokande experiment confirmed the existence of neutrino oscillations in high-energy solar neutrinos. Additionally, the KamLAND experiment in the early 2000s observed a clear oscillation pattern in the reactor neutrino spectrum.

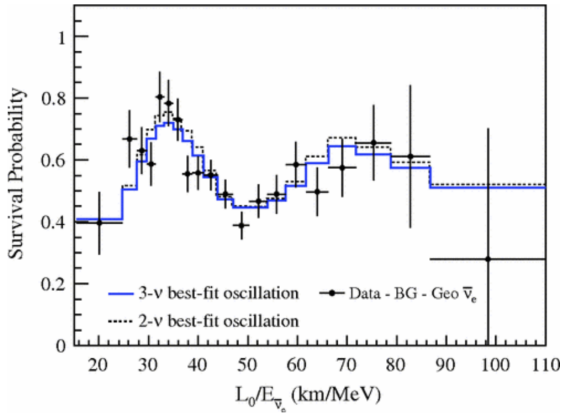

Figure 2.2: Oscillation in reactor neutrinos observed by KamLAND [2]

2.5.1 Theory of neutrino oscillations

Neutrino oscillation arises from simple quantum mechanics at play. In the standard model, the three neutrino flavor eigenstates form a complete orthonormal basis. Similarly, we can construct an eigen-basis

for the three mass states of neutrinos. After observing neutrino oscillations, it has been established that these two basis are not the same and are rotated relative to each other.

$$|\nu_\alpha\rangle = \sum_{k=1}^{3} U_{\alpha k}|\nu_k\rangle \tag{2.3}$$

where α = e, μ, τ and k = 1,2,3.
Or,

$$\begin{pmatrix}\nu_e\\ \nu_\mu\\ \nu_\tau\end{pmatrix} = \begin{pmatrix}U_{e1} & U_{e2} & U_{e3}\\ U_{\mu 1} & U_{\mu 2} & U_{\mu 3}\\ U_{\tau 1} & U_{\tau 2} & U_{\tau 3}\end{pmatrix}\begin{pmatrix}\nu_1\\ \nu_2\\ \nu_3\end{pmatrix} \tag{2.4}$$

The 3×3 matrix containing all $U_{\alpha i}$ is the neutrino mixing matrix known as the Pontecorvo-Maki-Nakagawa-Sakata (PMNS)matrix.

Parameterizing the PMNS matrix gives:

$$U = \begin{pmatrix} c_{13}c_{12} & c_{13}s_{12} & s_{13}e^{-i\delta_{CP}}\\ -c_{23}s_{12} - s_{23}c_{12}s_{13}e^{i\delta_{CP}} & c_{23}c_{12} - s_{23}s_{12}s_{13}e^{i\delta_{CP}} & c_{13}s_{23}\\ s_{23}s_{12} - c_{23}c_{12}s_{13}e^{i\delta_{CP}} & -s_{23}c_{12} - c_{23}s_{12}s_{13}e^{i\delta_{CP}} & c_{13}c_{23}\end{pmatrix} \tag{2.5}$$

where θ_{13}, θ_{23} and θ_{12} are 3 mixing angles, δ_{CP} is a CP-violating phase.

Initially, a neutrino from a weak interaction is in a superposition of mass eigenstates with different masses. These states acquire different relative phases over time, causing the neutrino's state to change and leading to its detection in a different state. Mathematically, the neutrino's state at time t can be written as:

$$|\nu_\alpha(t)\rangle = \sum_k U_{\alpha k}|\nu_k(t)\rangle \tag{2.6}$$

Solving the Schrödinger equation for the mass state, we get a plane wave solution:

$$|\nu_k(t)\rangle = e^{-\iota E_k t}|\nu_k\rangle \tag{2.7}$$

Transition probability $P(\nu_\alpha \to \nu_\beta)$ is given by:

$$\begin{aligned} P(\nu_\alpha \to \nu_\beta) &= |\langle\nu_\beta|\nu_{\alpha(t)}\rangle|^2\\ &= \sum_{k,j} U_{\alpha k}U^*_{\beta k}U^*_{\alpha j}U_{\beta j}e^{-\iota(E_k - E_j)t} \end{aligned} \tag{2.8}$$

We can approximate:

$$E_k \simeq E + \frac{m_k^2}{2E} \;\simeq\; p + \frac{m_k^2}{2E} \tag{2.9}$$

$$E_k - E_j \simeq \frac{\Delta m^2_{kj}}{2E} \tag{2.10}$$

where Δm^2_{kj} is the squared mass difference = $\Delta m^2_{kj} = m_k^2 - m_j^2$.

Propagation time 't' can be approximated to the distance traveled L. So, the oscillation probability becomes:

$$P(\nu_\alpha \to \nu_\beta) = \sum_{k,j} U_{\alpha k}U^*_{\beta k}U^*_{\alpha j}U_{\beta j}\exp\left(-\iota\frac{\Delta m^2_{kj}L}{2E}\right) \tag{2.11}$$

Separating imaginary and real terms we get:

$$\begin{aligned} P(\nu_\alpha \to \nu_\beta) \;= \delta_{\alpha\beta} \;-\; 4\sum_{k>j}\mathcal{R}\left(U_{\alpha k}U^*_{\beta k}U^*_{\alpha j}U_{\beta j}\right)\sin^2\left(\frac{\Delta m^2_{kj}L}{4E}\right)\\ + 2\sum_{k>j}\mathcal{I}\left(U_{\alpha k}U^*_{\beta k}U^*_{\alpha j}U_{\beta j}\right)\sin\left(\frac{\Delta m^2_{kj}L}{2E}\right) \end{aligned} \tag{2.12}$$

This shows that neutrino oscillations are dependent on the distance between the source and the detector (L) and neutrino energy (E), along with the PMNS matrix elements and mass squared differences, which are physical constants.

2.6 Neutrino oscillations in matter

In 1978, L. Wolfenstein pointed out that presence of matter affects neutrino oscillation [3]. All neutrino oscillation experiments on Earth except for reactor and short-baseline experiments, must account for matter effects, since neutrinos typically traverse significant amounts of Earth's interior. Similarly, solar neutrinos experience substantial matter effects as they propagate outward from their production sites in the Sun's dense core, passing through layers of solar material before reaching detectors on Earth.

Neutrinos undergo coherent forward scattering as well as incoherent scatterings in a medium. However, the effects of incoherent scatterings are negligible, if the mean free path of a neutrino is to be less than the diameter of earth, the neutrino should have about 10^5 GeV energy (which is a lot).

Ordinary matter has electrons but no muons or taus. An electron neutrino can interact with electrons via both charged and neutral current interactions, whereas muon and tau neutrinos can interact with electrons only via neutral current interaction. This causes an interaction potential to develop that modifies the effective mass of the neutrinos, thereby changing their wave functions.

2.7 Effective potentials in matter

There are 2 types of interaction potentials that arise depending upon whether the scattering was a neutral current scattering or a charged current scattering:

- V_{CC} **Potential due to Charged Current scattering:** This potential is formed when a ν_e exchanges a W boson with an e^- of the medium. It has to be obviously directly proportional to the electron number density N_e, and is also directly proportional to the Fermi coupling constant G_F.

  $$V_{CC} = +\sqrt{2}G_F N_e \tag{2.13}$$

  For antineutrinos the sign of V_{CC} changes.

- V_{NC} **Potential due to Neutral Current scattering:** Any neutrino can interact with an e- or a nucleon by exchanging a Z boson. This interaction is flavor independent. Contributions of electrons and protons cancel each other, so in a neutral medium V_{NC} will only depend on neutron number density N_n, and the Fermi coupling constant G_F.

  $$V_{NC} = -\frac{\sqrt{2}}{2}G_F N_n \tag{2.14}$$

  Again, for antineutrinos the sign of V_{NC} changes.

2.8 Evolution of neutrino flavors

These extra potentials modify the total Hamiltonian of a neutrino propagation. The Schrodinger equation for the propagation of a neutrino with initial state α in matter is given by:

$$\iota\frac{d}{dt}|\nu_\alpha(t)\rangle = \mathcal{H}|\nu_\alpha(t)\rangle \tag{2.15}$$

here, $\mathcal{H}$ is the total Hamiltonian of the system and is equal to:

$$\mathcal{H} = \mathcal{H}_0 + \mathcal{H}_M \tag{2.16}$$

with $\mathcal{H}_0$ being the Hamiltonian in vacuum and

$$\mathcal{H}_M|\nu_\alpha\rangle = V_\alpha|\nu_\alpha\rangle \tag{2.17}$$

where V_α is given by

$$V_\alpha = V_{NC} + V_{CC} \tag{2.18}$$

The probability that ν_α will oscillate to ν_β in time t is

$$P_{\nu_\alpha \to \nu_\beta}(t) = |\psi_{\alpha\beta}(t)|^2 = |\langle \nu_\beta | \nu_\alpha(t) \rangle|^2 \tag{2.19}$$

where $\psi_{\alpha\beta}(t)$ is the oscillation amplitude with $\psi_{\alpha\beta}(0) = \delta_{\alpha\beta}$. The time evolution equation for the flavor oscillation amplitudes is

$$\iota \frac{d}{dt}\psi_{\alpha\beta}(t) = \sum_\eta \left(\sum_k U^*_{\beta k} E_k U_{\eta k} + \delta_{\beta\eta} V_\beta \right) \psi_{\alpha\eta}(t) \tag{2.20}$$

It is possible to show that

$$\sum_\eta \psi_{\alpha\eta}(t)\psi^*_{\beta\eta}(t) = \delta_{\alpha\beta} \tag{2.21}$$

Again, using eqn(2.9) and t $\simeq$ x, because we only deal with ultrarelativistic neutrinos, we get evolution equation for neutrinos in space instead time:

$$\iota \frac{d}{dx}\psi_{\alpha\beta}(x) = \left(\mathbf{p} + \frac{m_1^2}{2E} + V_{NC} \right) \psi_{\alpha\beta}(x) + \sum_\eta \left(\sum_k U^*_{\beta k} \frac{m^2_{k1}}{2E} U_{\eta k} + \delta_{\beta e}\delta_{\eta e} V_{CC} \right) \psi_{\alpha\eta}(x) \tag{2.22}$$

In this expression, the first term is separated out because it can be eliminated by phase shift and doesn't affect the probability of oscillations. Hence, the relevant evolution equation is:

$$\iota \frac{d}{dx}\psi_{\alpha\beta}(x) = \sum_\eta \left(\sum_k U^*_{\beta k} \frac{m^2_{k1}}{2E} U_{\eta k} + \delta_{\beta e}\delta_{\eta e} V_{CC} \right) \psi_{\alpha\eta}(x) \tag{2.23}$$

We see that neutrino oscillations in matter depend on squared mass differences like they do in vacuum.

Writing eqn(2.23) in matrix form:

$$i \frac{d}{dx}\Psi_\alpha = \mathcal{H}_F \Psi_\alpha \tag{2.24}$$

The effective Hamiltonian is given by:

$$\mathcal{H}_F = \frac{1}{2E}(U\mathcal{M}^2 U^\dagger + \mathcal{A}) \tag{2.25}$$

where,

$$\mathcal{M}^2 = \begin{pmatrix} 0 & 0 & 0 \\ 0 & \Delta m^2_{21} & 0 \\ 0 & 0 & \Delta m^2_{31} \end{pmatrix} \quad \text{and} \quad \mathcal{A} = \begin{pmatrix} A_{CC} & 0 & 0 \\ 0 & 0 & 0 \\ 0 & 0 & 0 \end{pmatrix} \tag{2.26}$$

with $A_{CC} \equiv 2EV_{CC} = 2\sqrt{2}EG_F N_e$ and Ψ_α, the wave function is,

$$\Psi_\alpha = \begin{pmatrix} \psi_{\alpha e} \\ \psi_{\alpha\mu} \\ \psi_{\alpha\tau} \end{pmatrix} \tag{2.27}$$

2.9 The MSW effect

If a neutrino is passing through a medium of variable density, then mixing of neutrinos will grow to maximum at some value of the electron density and then will turn back.

Considering the simplest case of two neutrino mixing, effective neutrino oscillation parameters in matter become:

$$\Delta m^2_M = \sqrt{\left(\Delta m^2 \cos 2\theta - {\mathrm{A_{CC}}}^2\right) + \left(\Delta m^2 \sin 2\theta\right)^2} \tag{2.28}$$

and

$$\tan 2\theta_M = \frac{\tan 2\theta}{1 - \frac{\mathrm{A_{CC}}}{\Delta m^2 \cos 2\theta}} \tag{2.29}$$

Mikheyev and Smirnov in 1985 pointed out that when A_{CC} becomes equal to $\Delta m^2 \cos 2\theta$, there is a resonance in mixing because then effective mixing angle becomes equal to $\pi/4$, i.e., the mixing is maximal [4]. This leads to the possibility of complete oscillations between two flavors. This resonant effect of matter is called MSW effect or MSW Resonance.

Note that effective Δm^2 in matter has its minimum value at resonance.

$$\Delta m^2_M|_R = \Delta m^2 \sin 2\theta$$

Also note that A_{CC} is positive for normal matter and θ is $< \pi/4$ because for $\theta > \pi/4$ we have $\cos 2\theta < 0$.

Chapter 3

Geoneutrinos

This chapter introduces to the concept of geoneutrinos and the information they can tell us about their astrophysical parent body - Earth. Section 3.1 presents an overview of the Earth's radiogenic heat production. Section 3.2 deals with the understanding of geoneutrinos and their production, propagation and eventual detection in the detectors. Section 3.3 explains the latest geoneutrino results from KamLAND and Borexino with a brief discussion of the uncertainties in those results.

3.1 Earth's Radiogenic heat production

Heat flux from the Earth's surface is 47 ± 3 TW [5]. It is the highest among all of the terrestrial planets. 2 major processes - (1) primordial cooling from Earth's accretion and (2) decay of long-lived radioactive isotopes, contribute to the net output power of Earth. However, the precise individual contribution of each remains uncertain. Earth loses heat through secular cooling and produces heat through decay of radioactive elements. Knowing the relative contribution of these 2 processes tells us about the heat budget of the Earth. In the second half of the 19th century, Lord Kelvin tried to calculate the age of the Earth from the surface heat flux and found it to be bizzaringly small [6]. He hypothesized the existence of a source of heat production within Earth and attributed it to the chemical energy of reaction of substances forming the Earth. However, later when radioactivity was discovered, it was established that the Earth produces some heat through radioactive decays of elements such as uranium U-238, thorium Th-232, and potassium K-40 contained within it. Such elements are also called Heat Producing Elements (HPEs). Radiogenic heat has slowed down the overall cooling of the Earth since its formation. When the Earth was young, it produced much more heat than it does now due to the existence of short lived radioisotopes that have gone now extinct. It is the long lived radioisotopes that contribute to the heat production. Although the rate of primordial cooling is relatively slow, without the additional contribution of radiogenic heat from the decay of HPEs, the Earth would have lost most of its internal heat early in its history and become geologically inactive. This heat influences mantle convection, drives plate tectonics, and plays a critical role in the geodynamo that generates Earth's magnetic field. Hence, constraining the radiogenic heat budget of the Earth is crucial.

3.1.1 Compositional models of Earth

36 refractory elements exist in constant ratios to each other. U and Th are 2 of these. Knowing the absolute abundance of any one of the 36 gives the abundance of all others.

To estimate Earth's total radiogenic heat, geoscientists rely on models of the Bulk Silicate Earth (BSE), which represents the composition of the Earth's mantle and crust, excluding the metallic core. Several BSE models have been proposed but we can broadly classify them in 3 according to their prediction on the amount of radiogenic heat produced in Earth:

Low heat (Q) model — Derived from enstatite chondrites, they predict lower abundances of U and Th, resulting in about 11 TW of radiogenic heat.

Middle heat (Q) model — Based on the composition of chondritic meteorites, these suggest a moderate radiogenic heat production of about 20 TW and are supported by mantle-derived samples.

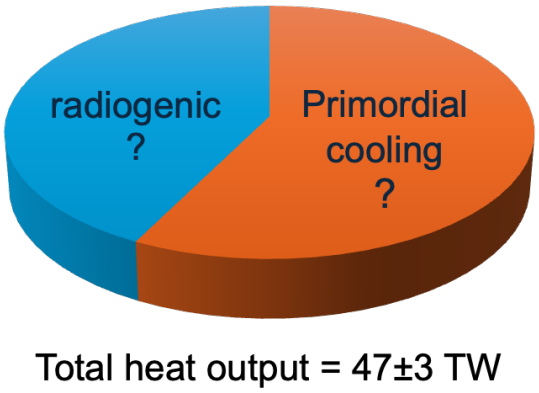

Figure 3.1: Earth as a hybrid engine fueled by primordial and radiogenic heat

High heat (Q) model — These balance the energy needed for mantle convection, implying higher radiogenic heat production, up to 35 TW.

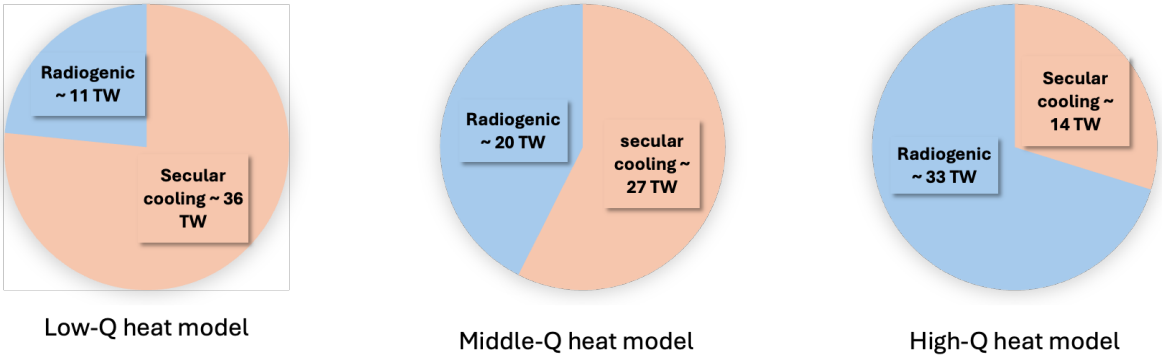

Figure 3.2: Heat models

However, direct measurement of the radiogenic heat or verifying the compositional models of Earth is challenging due to the inaccessibility of the whole Earth. Here, geoneutrinos provide a direct and absolute probe into Earth's interior, offering a way to estimate the abundances of heat-producing elements and thereby constraining the radiogenic heat production of the Earth.

3.2 Geoneutrinos as a tool to understand composition and heat budget of Earth

Geoneutrinos are electron antineutrinos $\bar{\nu_e}$ emitted during the radioactive decay of U-238, Th-232 (chains) and K-40 inside Earth. These neutrinos escape the Earth's interior without significant interaction, carrying important geophysical information with them.

The geoneutrino flux of Earth from the most widely accepted compositional model of the Bulk Silicate Earth is about 10^6 $\bar{\nu}_e/cm^2/s$.

$$
\begin{aligned}
^{238}\mathrm{U} &\rightarrow {}^{206}\mathrm{Pb} + 8\alpha + 6e^- + 6\bar{\nu}_e + 51.7\,\mathrm{MeV} \\
^{232}\mathrm{Th} &\rightarrow {}^{208}\mathrm{Pb} + 6\alpha + 4e^- + 4\bar{\nu}_e + 42.7\,\mathrm{MeV} \\
^{40}\mathrm{K} &\rightarrow {}^{40}\mathrm{Ca} + e^- + \bar{\nu}_e + 1.311\,\mathrm{MeV}
\end{aligned}
$$

The idea of extracting geological information from the antineutrinos produced inside Earth by HPEs was first proposed by Krauss et al. in 1984 [7].

About 20 years later, the KamLAND experiment in Japan reported the first measurement of geoneutrino flux [8] followed by the Borexino detector in Italy in 2010 [9].

3.2.1 Geoneutrino flux

The differential flux of geoneutrinos at a spatial point $\vec{r}$ can be expressed as:

$$\frac{d\Phi(E_\nu, \vec{r})}{dE_\nu} = \sum_{i \in \{\mathrm{U,Th}\}} A_i \cdot \frac{dN_i}{dE_\nu} \int_{\mathrm{Earth}} \frac{a_i(\vec{r}\,')\,\rho(\vec{r}\,')}{4\pi|\vec{r} - \vec{r}\,'|^2}\, P(E_\nu, |\vec{r} - \vec{r}\,'|)\, d^3\vec{r}\,' \tag{3.1}$$

Here, A_i represents the number of electron antineutrinos ($\bar{\nu}_e$) produced per decay of isotope i. The term $\frac{dN_i}{dE_\nu}$ denotes the energy spectrum of emitted $\bar{\nu}_e$ for each decay mode. The quantity $a_i(\vec{r}\,')$ corresponds to the number of atoms of the radioactive isotope per unit mass of rock at position $\vec{r}\,'$, and $\rho(\vec{r}\,')$ is the local rock density. The function $P(E_\nu, |\vec{r} - \vec{r}\,'|)$ gives the survival probability of $\bar{\nu}_e$ traveling a distance $|\vec{r} - \vec{r}\,'|$ with energy E_ν.

Due to the spatial averaging over distances much larger than the $\nu_1 - \nu_2$ oscillation length and the limited energy resolution of detectors such as KamLAND, the oscillation-induced variations are effectively averaged out. As a result, a constant average survival probability of

$$P_{ee} = 0.554^{+0.012}_{-0.009} \tag{3.2}$$

is used in the calculation.

The total geoneutrino flux at location $\vec{r}$ is then obtained by integrating the differential flux over the energy spectrum:

$$\Phi(\vec{r}) = \sum_{i \in \{\mathrm{U,Th}\}} A_i \cdot N_i \int_{\mathrm{Earth}} \frac{a_i(\vec{r}\,')\,\rho(\vec{r}\,')}{4\pi|\vec{r} - \vec{r}\,'|^2}\, P_{ee}\, d^3\vec{r}\,' \tag{3.3}$$

In this expression, N_i is the total number of $\bar{\nu}_e$ emitted per decay chain of isotope i.

3.2.2 Detection techniques

Geoneutrinos are detected through inverse beta decay (IBD) process in kiloton-scale liquid-scintillator detectors such as KamLAND and Borexino. In this channel, an electron antineutrino interacts with a free proton in the hydrocarbon scintillator, producing a positron and a neutron. The energy threshold for the electron antineutrino required for this reaction is 1.806 MeV. The positron deposits its kinetic energy and promptly annihilates, emitting two 511 keV γ-rays that generate a scintillation flash whose total light yield encodes the antineutrino energy. After drifting a few centimeters, the neutron is captured, typically on a proton (yielding a 2.2 MeV γ after about 200 μs). This prompt plus delayed time and space coincidence forms an unmistakable IBD signature that suppresses natural-radioactivity backgrounds by several orders of magnitude. The difficulties include obtaining a measurable geoneutrino signal of only several dozen occurrences per kiloton-year and the spectral interference with reactor antineutrinos. These issues are addressed by situating detectors at a distance from nuclear power stations, applying deep underground shielding to diminish cosmogenic spallation, and employing accurate energy reconstruction methods to distinguish spectra derived from U and Th from those of reactor and other background sources.

Current detection technologies only allow the measurement of antineutrino flux from U and Th, since the energy of antineutrinos from K-40 is below the detection threshold.

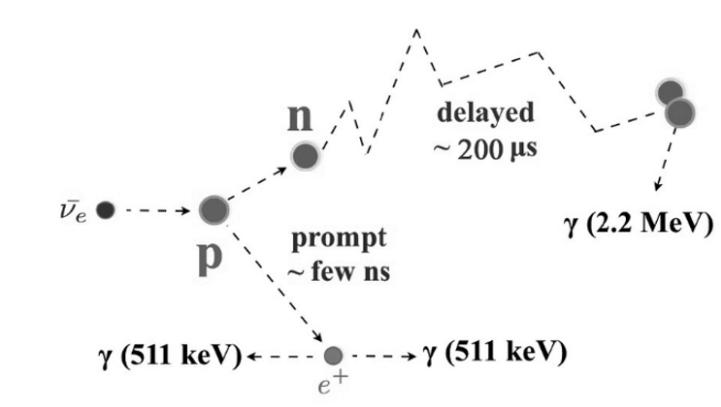

Figure 3.3: Inverse beta decay process

3.3 Current geoneutrino flux results from recent experiments

KamLAND - Kamioka Liquid Scintillator Anti-Neutrino detector is a neutrino detector built inside the Kamioka mine in Hida, Gifu, Japan. KamLAND was originally built to detect neutrino oscillations from reactor neutrinos. After the 2011 earthquake, Japanese reactors were shut off, which offered a reactor neutrino free period for observing geoneutrinos in KamLAND. The latest geoneutrino result from KamLAND after data taking of more than 18 years including the reactor off period is consistent with compositional models of the Earth predicting low to medium radiogenic heat (10 - 20 TW) [10].

While from the latest results from Borexino, the estimated radiogenic power is $38.2^{+13.6}_{-12.7}$ TW [11]. However, this result was later reanalyzed incorporating the U,Th rich local crust of the Borexino detector and an estimate of roughly 20 TW of overall radiogenic power from U, Th and K was concluded [12].

3.3.1 Uncertainties in the results

Uncertainties in TW estimates arise from the lack of accurate models of the surrounding crust, approximately 500 km around detectors. Detector sensitivity decreases with distance in an inverse square manner, so the observed flux primarily comes from the uncertain local lithosphere. By applying a local geological model to the detected geoneutrino flux and combining it with a global model, we estimate the mantle's radiogenic power after subtracting the local contribution. So we can consider the crust and mantle signals to be 2 unknowns.

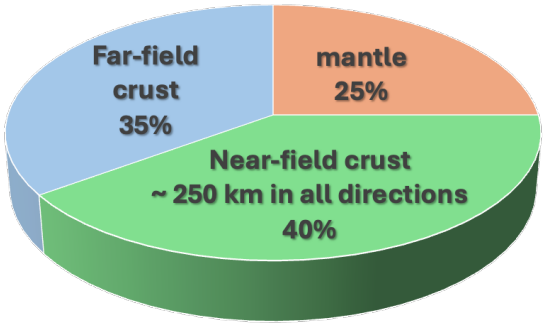

Figure 3.5: Contributions to geoneutrino flux at a land based detector

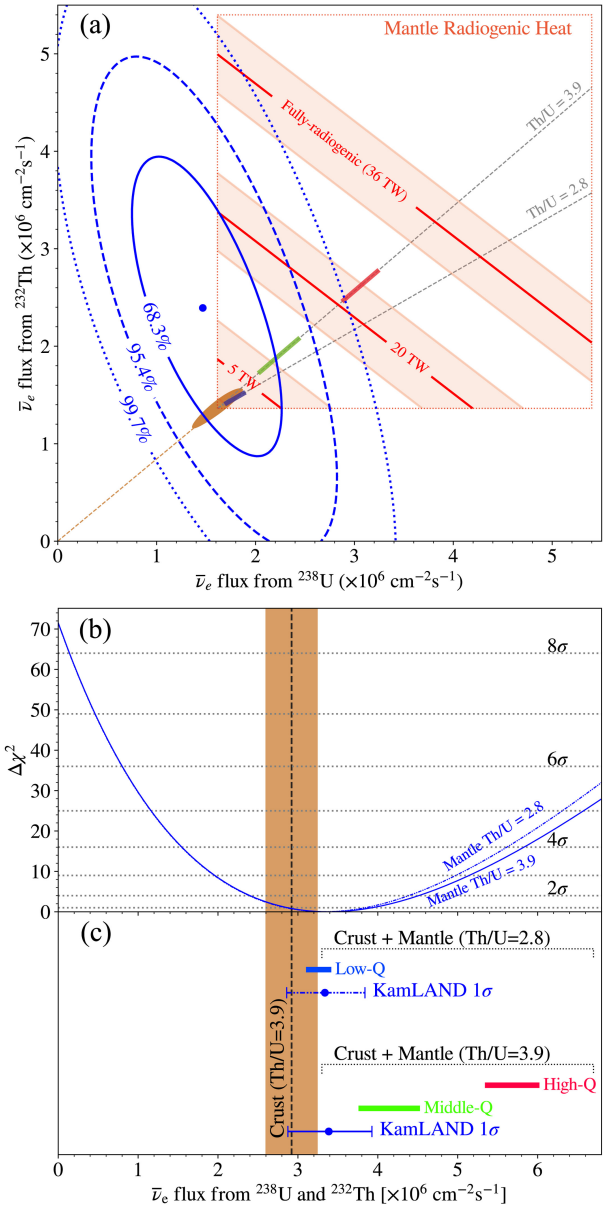

Figure 3.4: Estimation of Earth's radiogenic heat model from KamLAND's latest geoneutrino flux measurements

3.4 Looking forward: mantle geoneutrinos measurement from ocean floor

Given the reliance of crustal and mantle geoneutrino signal determination on variable local and global geological models, isolating the mantle signal could prove beneficial in resolving this puzzle. Raghavan et al in 1998 [13] first proposed the idea to measure the mantle flux from the oceans.

Future efforts aim to deploy a geoneutrino detector on the ocean floor, where the thinner oceanic crust and reduced crustal radioactivity can provide a clearer look into mantle geoneutrino flux.

Proposed projects, such as the Hanohano detector in the past and Ocean Bottom Detector in the present envision a mobile, deep-ocean liquid scintillator detector capable of being placed at multiple locations to map geoneutrino flux globally. The deep ocean setting offers the following advantages:

- Minimal overlying crust reduces crustal background
- Deep water provides shielding from cosmic ray induced backgrounds

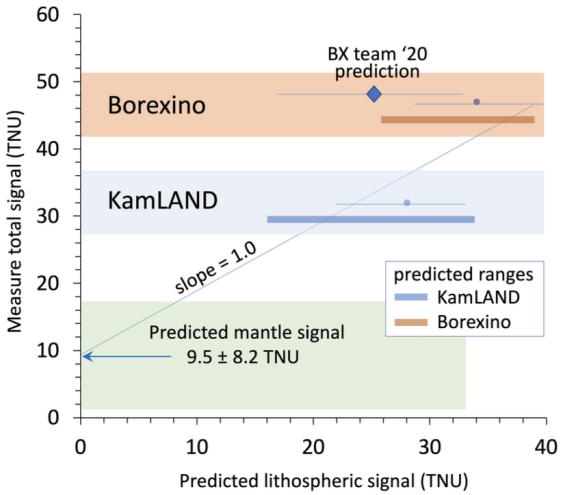

Figure 3.6: Model predictions for the geoneutrino signal at KamLAND and Borexino and predicted mantle flux [14]

- Mobile deployment enables sampling at diverse mantle locations

Achieving these goals requires overcoming significant engineering challenges, including detector stability at high pressures, long-term operation in remote environments, and data transmission to shore.

In summary, geoneutrinos represent a unique intersection between particle physics and geoscience. Their study provides a direct, non-invasive probe of Earth's interior, complementing traditional geochemical and geophysical methods, and holds the promise of answering fundamental questions about the composition and energy balance of our planet.

Chapter 4

Ocean Bottom Neutrino Detector

As explained in the previous chapter, measuring mantle geoneutrinos from the ocean floor is the next step in furthering the geoneutrino science.

In the past, University of Hawaii and the Makai Ocean Engineering in 2005 concieved the idea of deploying a neutrino detector - Hanohano in the sea but the idea was never realized.

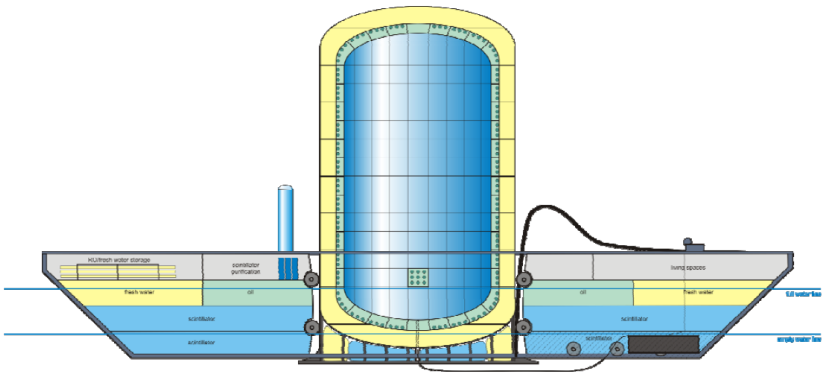

Figure 4.1: Hanohano detector conceptual design

For a long time the idea was not taken up by the scientific community but in 2019, Tohoku University and JAMSTEC (The Japan Agency for Marine-Earth Science and Technology) started a collaborative effort to realize the idea of the Ocean Bottom Detector (OBD). The goal is to place a liquid scintillator neutrino detector on the ocean floor off the coast of Hawaii in the middle of the Pacific Ocean to measure a significant flux directly from the mantle.

The ultimate scientific objectives of this project are:

- direct constraints on Earth's mantle heat budget,
- improved models of geochemical reservoirs
- a better understanding of planetary evolution

4.1 Detector Design

The exact design of the detector is yet under study and is open to changes with upcoming better technologies in neutrino detections, the following is the design of a 1.5 kt detector used in some previous simulation studies.

It is a structure with the following main components:

Figure 4.2: Concept of Ocean Bottom Detector

Inner Detector

Inner detector consists of 1.5 kt liquid scintillator in an acrylic container. Neutrinos are detected within this volume through inverse beta decay process.

Buffer oil

To prevent the radioactivity from PMTs reaching the inner detector, all the PMTs are kept in a buffer volume which is filled with an optically compatible buffer oil. This region acts as a shield for the inner detector from external radiation.

PMT modules

Scintillation light produced in the LS region reaches the photomultiplier tubes which is then converted to electrical signals. The PMTs are to be housed in pressure resistant housings so as to protect them from the high pressure of the surroundings. They should also me made to consume as less power as possible.

Stainless steel tank

It is the outermost container of the detector. Stainless steel is the most optimal choice since it is corrosion resistant and is strong enough to withhold the pressure differences of inside vs outside.

Outer detector

Seawater surrounding the detector acts as the veto region to identify cosmic-ray muons entering the detector. Since muons can produce spallation products that mimic neutrino signals, tagging and vetoing these muon events is essential to reduce background. PMT modules will be employed in the seawater surrounding the detector like in KM3NeT detector which can also be used to study ultra high energy physics events in the future.

4.2 Strengths of OBD

Location - Ocean floor

The benefits of positioning a neutrino detector on the ocean floor include the fact that the oceanic crust is substantially thinner than the continental crust, containing fewer radioactive materials. This reduction in materials is expected to decrease contributions from the crust, making it easier to detect neutrinos with less interference and increased sensitivity to signals from the mantle.

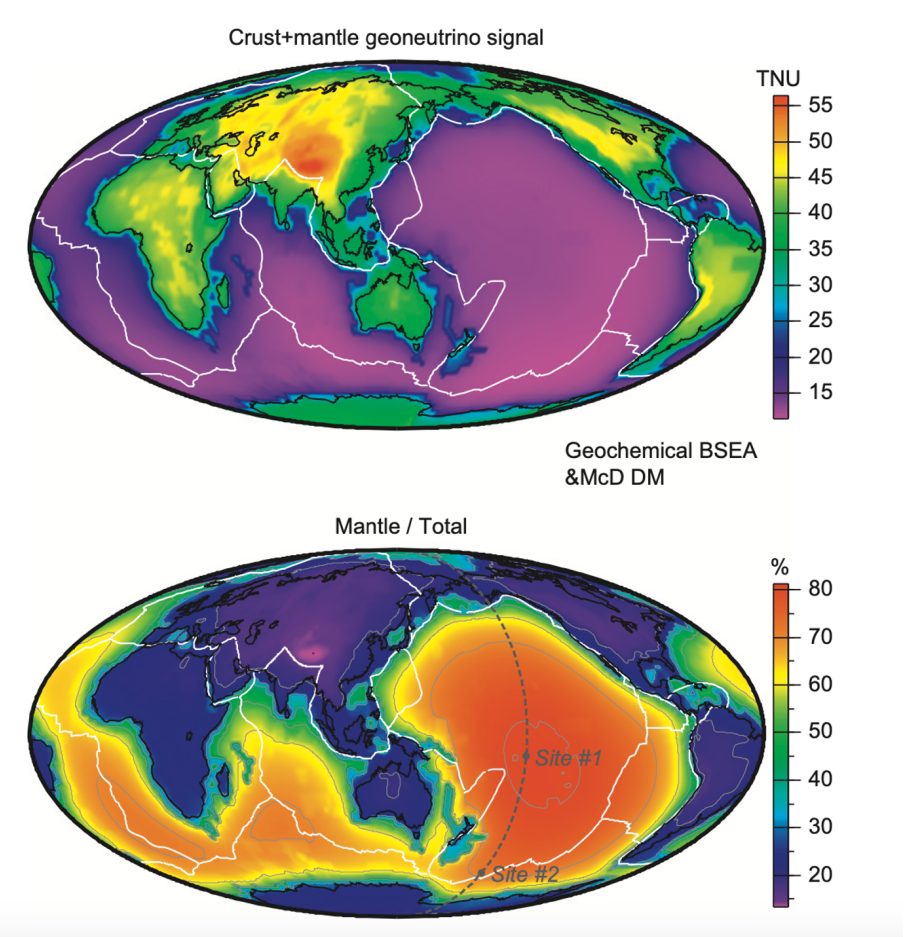

Figure 4.3: Distribution of geoneutrino signals on Earth [15]

Far from nuclear reactors

Additionally, placing the detector far from nuclear reactors reduces background noise from reactor neutrinos, enhancing the ability to study natural neutrino sources and engage in foundational research in neutrino physics.

Exploring structures within Earth

There are some distinct features in the Earth's mantle. Among them are the Large Low Shear Velocity Provinces (LLSVPs), massive structures located at the base of the mantle beneath Africa and the Pacific Ocean. They were detected through seismic tomography. They exhibit slower seismic wave speeds, indicating that they may be compositionally distinct and thermally anomalous compared to the surrounding mantle. These features are believed to influence mantle convection, plume formation, and Earth's thermal evolution. If the Ocean Bottom Detector is equipped with angular resolution, with sufficient sensitivity, it can be a promising tool to study these structures.

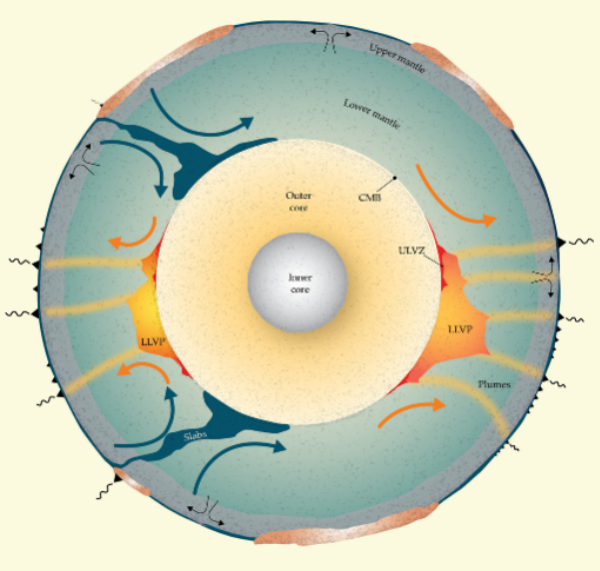

Figure 4.4: Two continent sized LLSVPs sitting in the lower mantle of the Earth [16]

Mobile detector - varying baseline

One unique advantage of having a large neutrino detector in the ocean is that it can be moved and deployed at different locations for certain periods of time. Although it is an extremely ambitious proposal, but it offers a unique advantage that no other neutrino detectors can offer which is a varying baseline. Neutrino oscillations can be studied over a number of different distances from reactors.

A mobile detector can also prove to be useful in nuclear non proliferation and safeguard applications.

Chapter 5

A deep sea liquid scintillator detector prototype module

A prototype module incorporating a liquid scintillator, photodetection modules, and supporting components is currently under development. This chapter presents an overview of its design, technical specifications, and the objectives of its deployment, particularly focusing on its operation in the deep sea environment.

5.1 Introduction

The prototype is a liquid scintillator (LS) detector coupled to photomultiplier tubes (PMTs), designed to detect radiation events by converting the energy into scintillation light, which is then recorded by the PMTs.

Unlike conventional laboratory- or land-based detectors, this module is specifically engineered to operate in a deep-sea environment, where it must withstand challenges such as high hydrostatic pressure and low temperatures. To ensure the detector's stability and functionality over extended periods on the seafloor, additional engineering measures have been implemented, including robust housing, pressure-resistant glass spheres for PMT modules, and pressure-volume compensation systems.

As an initial performance test, the detector is intended to operate continuously for a three-month observation period on the ocean floor. This long-term deployment will evaluate the stability of both the LS+PMT system and the supporting equipment under real oceanic conditions.

5.2 Objectives

The primary objective of deploying this prototype to the seafloor is to test the feasibility of an ocean-based liquid scintillator detector. Specifically, the deployment will assess:

1. **Technology Demonstration in a Compact Detector:**

   This deployment aims to demonstrate and validate the technologies developed for deep sea neutrino detection, including photomultiplier tube (PMT) modules, data acquisition systems (DAQ), underwater connection systems, and a pressure compensation mechanism. The integration and coordination of these components will be thoroughly tested to ensure their reliability and robustness in harsh marine conditions. Particular emphasis will be placed on verifying mechanical integrity under high hydrostatic pressure, ensuring watertight sealing and pressure balance in PMT glass housings, and confirming that the pressure compensation system responds effectively to gradual thermal and pressure induced density changes in the liquid scintillator. The DAQ chain, from optical signal conversion in the PMTs to digitization and transmission via the cabled observatory, will be monitored for timing stability, synchronization accuracy, and noise resilience. Additionally, the underwater connector system will be evaluated for ease of mating/demating via remotely operated vehicles (ROVs), electrical contact reliability, and resistance to corrosion or mechanical wear

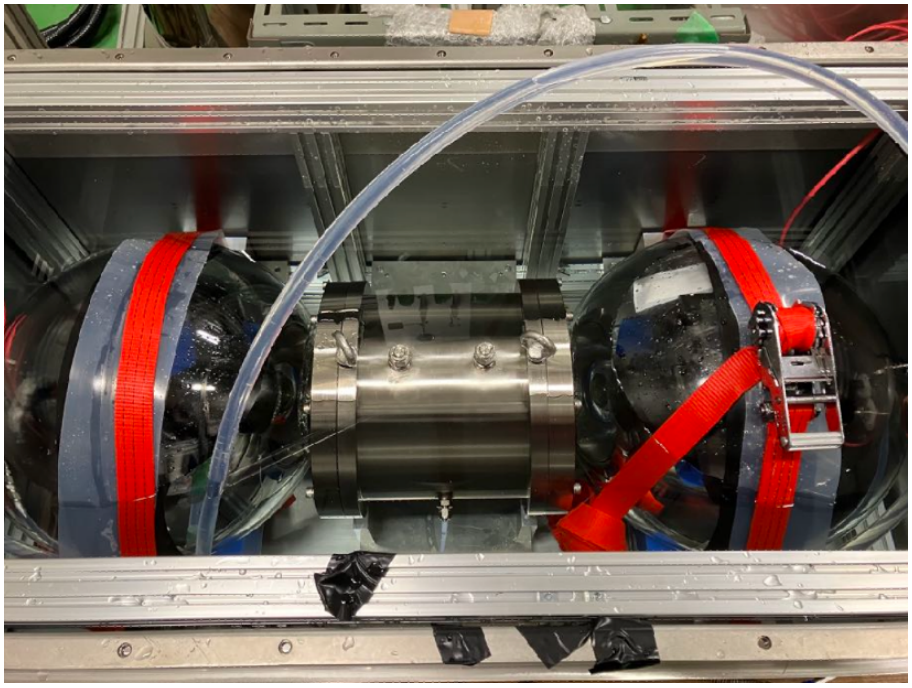

Figure 5.1: Prototype detector (open from the top)

over repeated operations. Successful validation of these systems in an integrated configuration will confirm that the prototype meets the operational demands of sustained deep sea neutrino detection.

2. **Long-Term Stability Test:** The prototype detector will undergo continuous deployment for approximately three months at the JAMSTEC Hatsushima Observatory, a period longer than the typical few weeks to one month of most operations at this site with exceptional cases of few years [17, 18, 19]. This timeframe is subjected to change by the available ship time of research vessels responsible for the installation and uninstallation of the prototype on the seafloor. This extended duration provides a rare opportunity to evaluate the detector's stability under realistic seafloor conditions. Throughout the run, detector performance parameters such as light yield, energy resolution, and PMT gain will be monitored, while environmental effects including biofouling, sedimentation, and small seawater temperature fluctuations (less than 1°C at Hatsushima [20]) will be tracked. Moreover, immediately after deployment, the detector will gradually equilibrate to the ambient deep-sea temperature (2–4°C), allowing us to monitor its response during this transient cooling phase and quantify temperature dependent variations in scintillator light yield and PMT gain collectively. The three month timeframe also allows to test the robustness of continuous power delivery through the supply cables and the long-term stability of electronics under sustained hydrostatic pressure (∼10 MPa). Since most early-life instabilities in electronics or power systems should typically emerge within hours or days of initializing the operation, demonstrating uninterrupted functionality over several months establishes confidence that the system can be scaled to year-scale deployments. In addition, the extended observation period enables assessment of periodic or episodic marine influences, such as tidal cycles, underwater currents, or seismic events, which could affect detector alignment, mechanical stress, or noise levels in the data. Collectively, these evaluations will provide essential baseline data for designing a larger, longer duration ocean bottom neutrino detector.

3. **Regular Calibration Runs:**

   To evaluate the impact of environmental factors on the detector's performance, regular calibration runs using a Cs-137 gamma calibration source will be conducted. These calibrations will track variations in detector gain, photon yield, and energy resolution over time, providing quantitative indicators of performance drift. By maintaining a consistent calibration geometry and source activity, it will be possible to distinguish between environmental influences such as minor seawater temperature fluctuations, pressure effects on PMT response, or light transmission changes in optical interfaces and intrinsic detector degradation. Daily baseline monitoring will complement scheduled

calibration runs, enabling the detection of short term variations potentially caused by tidal pressure cycles, underwater currents, or microseismic events. The calibration data will also serve as an ongoing validation of simulation models, ensuring that optical photon transport and PMT response in the deep sea environment remain within predicted tolerances. This integrated calibration and monitoring strategy will strengthen confidence in the detector's stability assessments and inform the design of calibration protocols for future large-scale ocean-based detectors.

The successful realization of these objectives will mark an essential step towards scaling up this prototype into a larger, distributed array suitable for a next generation ocean based neutrino observatory.

5.3 Design and specifications

5.3.1 Components

Outer stainless steel tank

The prototype detector will be housed inside a stainless steel tank of dimensions:
$1.326 \times 0.666 \times 0.636\ m^3$

It houses all the components of the prototype module and is filled with seawater to make sure the pressure inside it remains the same as the surroundings.

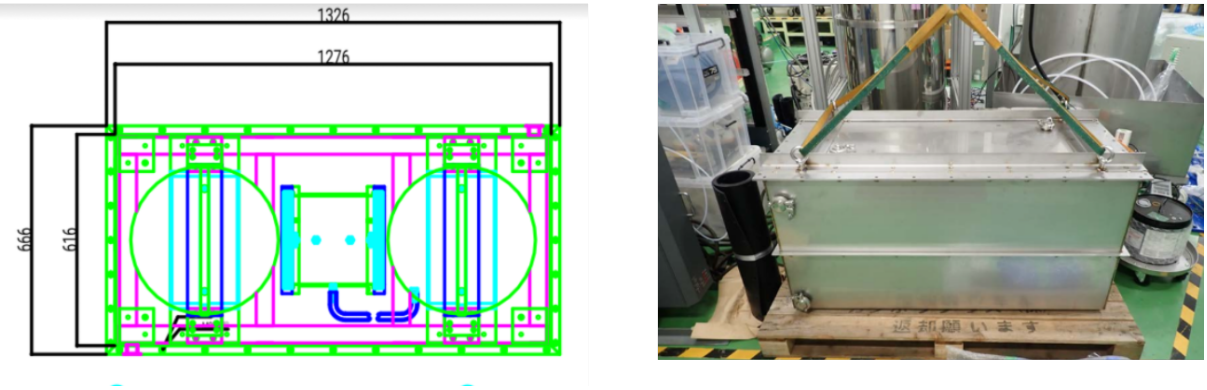

Figure 5.2: Outer stainless steel container

Liquid scintillator vessel

A cylindrical tube-like vessel made of stainless steel is designed to store the liquid scintillator. Its diameter is 26 cm and length is 20 cm.

This vessel can contain about 12 liters of liquid scintillator. The inner walls of the vessel are polished to make them more reflective than usual stainless steel surfaces.

The 2 sides of the tube are flanged and acrylic plates are used as the viewports. The diameter of the acrylic plates is 30 cm and the thickness is 3 cm. The optical properties of acrylic are such that it allows the scintillation light to pass through it.

A rubber gasket is used at the joint of acrylic plates to the flanged part of the tubes, to make the connection leak-proof.

Figure 5.3: Stainless steel cylindrical vessel for liquid scintillator

Liquid scintillator

The scintillation process has long been used as one of the earliest methods for detecting ionizing radiation. When certain materials are excited by ionizing radiation, they emit scintillation light. This property has facilitated the detection and spectroscopy of various forms of radiation through the use of scintillation techniques.

For detectors with a kilotonne-scale capacity, organic liquid scintillators have always been the optimal choice. As previously metioned, the detection of geoneutrinos has exclusively been accomplished through scintillation light detection techniques. Both KamLAND and Borexino employ organic liquid scintillators as their primary detection media. Following this precedent, the Ocean Bottom Detector also intends to use organic liquid scintillator in its detection processes. Nevertheless, it is noteworthy that no prior experiments have employed organic liquid scintillators in marine environments. Alteratively, experiments such as KM3NeT and IceCube exploit their natural environments (seawater and ice, respectively) as the detection medium. Consequently, further studies into the application of organic liquid scintillators in marine settings are necessary.

Preliminary studies [21] have identified a combination of linear alkylbenzene (LAB) as a solvent and ppo as a solute as the chosen composition for the prototype detector.

Behavior of the LS cocktail in low temperatures of about 4° C has been studied and it was found that on reducing the temperatures, there appears cloudiness in the liquid which can be eliminated by bubbling dry nitrogen in the solution which suggests that the cloudiness comes from the moisture trapped in the solution.

Another interesting fact was found that the light yield of the LAB+ppo solution increases with decrease in temperature.

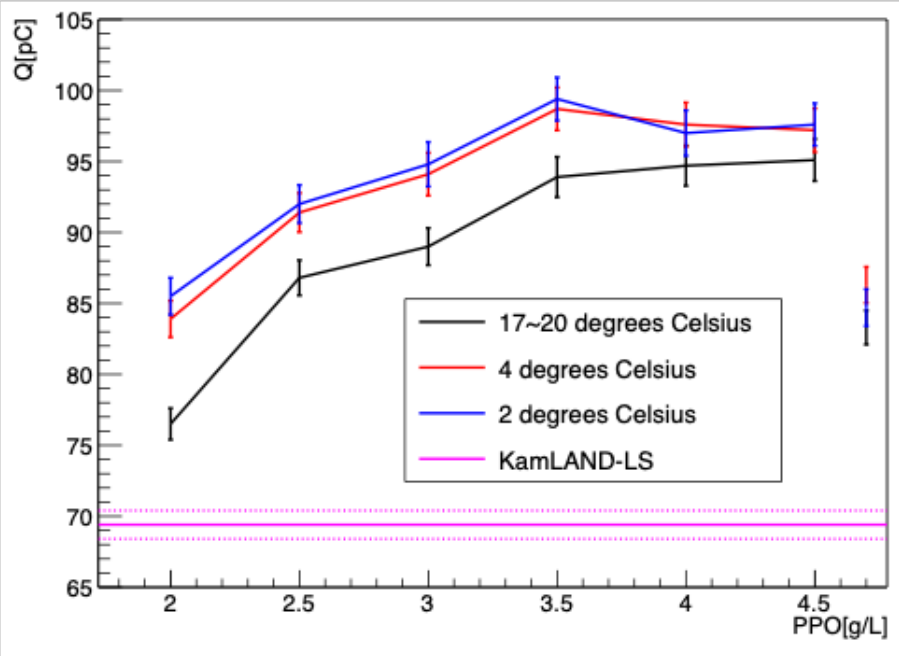

Figure 5.4: LAB+ppo light yield variation with temperature and ppo fraction

Photodetector Modules

To convert scintillation light into electrical signals, the prototype detector uses two photomultiplier tubes (PMTs) enclosed in robust, low radioactivity glass housings developed by Okamoto Glass to withstand deep sea pressure, following approaches used in experiments like KM3NeT and IceCube.

Potential Use of D-Egg Optical Modules

Dual Optical sensors in an ellipsoid glass for gen2 IceCube, in short D-Egg is the next generation optical module for the IceCube experiment at the South Pole. Its potential utilization with suitbale geometry in the prototype detector is being studied in an ongoing collaboration with Chiba University.

While the prototype detector simulations in this study (e.g., Fig. 6.13) have been performed assuming conventional spherical glass shields, the potential application of D-Egg type modules is also being considered for future iterations of the design.

D-Egg combines the PMT, protective glass housing, and integrated electronics in a compact unit, and can incorporate environmental sensors for internal pressure, temperature, tilt (via accelerometers), magnetic field, and light. This would provide the prototype detector with a packaged design of photodetector modules that improves both deployment and data collection. D-Egg houses 8 inch PMTs which offer increased surface area for light collection. Analytically, light collection efficiency increases to 11% on using the D-Egg module. Their high quantum efficiency would also improve the overall optical performance of the prototype detector.

Advantages of using D-Egg modules:

- Proven operation under very high pressure (up to 70 MPa), exceeding requirements for the planned deployment depth.
- Integrated data acquisition electronics within the module, reducing cabling complexity.
- Built-in environmental monitoring systems (temperature, pressure, tilt, magnetic field, light).
- Increased light collection efficiency and higher PMT quantum efficiency.

Improvement points required for use in the prototype detector

- The prototype currently uses one PMT per optical module, while the D-Egg houses two PMTs; the mechanical and electronic interfaces would need redesign.

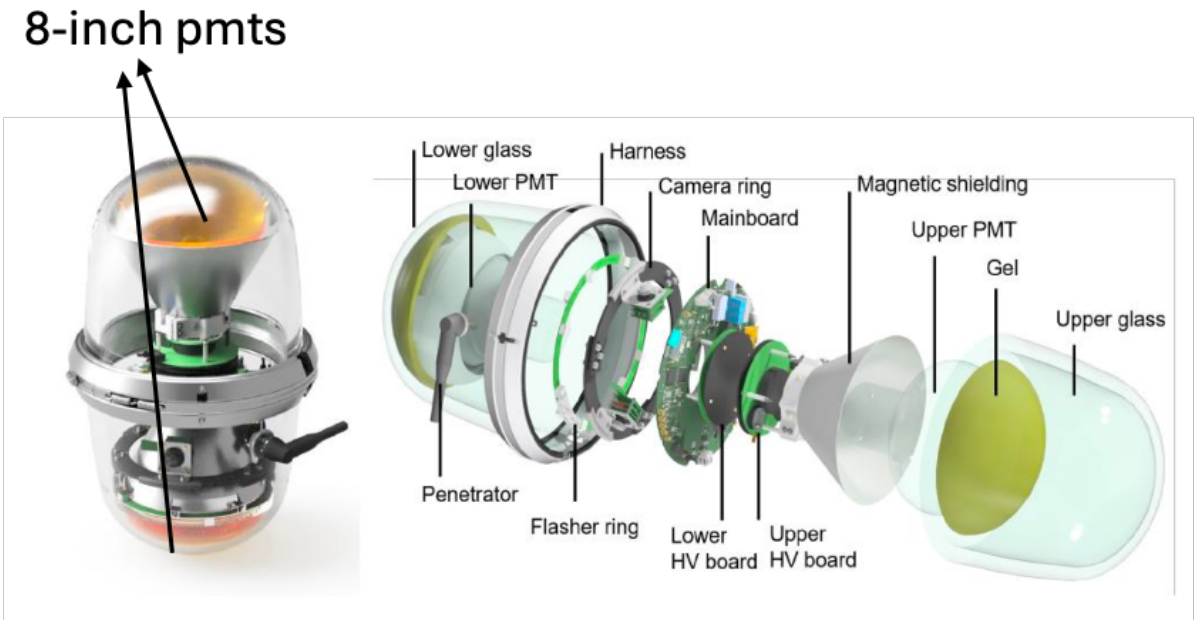

Figure 5.5: D-Egg and its internal components [22]

- Data taking software must be adapted to the D-Egg's integrated electronics and sensor systems.
- The module and its systems must be tested for stable operation in marine temperatures ($2° - 4°$C), since modules are designed to work in ultra cold temperatures of South Pole's ice.

At present, spherical glass shields are planned for the prototype deployment to fit within the stainless steel tank geometry and comply with the maximum hanging weight constraints of the deployment vessel. The evaluation of D-Egg integration is therefore treated as a forward looking study for potential upgrades, rather than an assumption in the current detector simulations.

A simplified optical performance comparison using D-Egg sized PMTs is presented in Section 6.3.1. This comparison modifies only the light collection parameters while retaining the spherical shield geometry, to illustrate the potential gains in photon collection efficiency without implying that the current simulations assume the D-Egg mechanical design.

Pressure Compensation Mechanism

Liquids exhibit finite compressibility when subjected to external pressure. At an ocean depth of approximately 1 km, the hydrostatic pressure reaches about 10 MPa. Under these conditions, the volume of the liquid scintillator can decrease by up to 2.1%. Such a reduction in active volume could adversely affect the detector's mechanical integrity and stability if left uncompensated. To address this issue, a pressure compensation mechanism has been developed. The system consists of a flexible hose connected to the liquid scintillator vessel, designed to act as a reservoir for additional scintillator. As external pressure compresses the main volume, the stored liquid in the hose is automatically supplied into the vessel, thereby maintaining the total scintillator volume close to its nominal value throughout deployment [23]. This approach ensures operational stability of the optical target region over extended periods in deep sea conditions.

Figure 5.6: Hose setup for pressure compensation system

5.4 Deployment location

The prototype detector is set to be deployed in the ocean at the JAMSTEC's Hatsushima deep sea cabled observatory [24].

The Hatsushima Observatory is a deep-sea floor observatory located in Sagami Bay, Japan, about 7 km off the coast of Hatsushima Island. It was established in 1993 at a depth of 1,175 meters to monitor seismic activity and other geophysical phenomena, with a focus on real time data collection. The observatory has been upgraded and renovated over the years, including the addition of various sensors and the implementation of underwater mateable connectors for future expansion [17].

The observatory is equipped with a variety of instruments, including:

- Video cameras: To observe biological activity and mudflows.
- Seismometers: To detect earthquakes.
- Hydrophones: To record underwater sounds.
- CTD sensors: To measure conductivity, temperature, and depth.
- Electromagnetic current meters: To measure water currents.
- Sub-bottom thermometers: To measure temperature at different depths.
- Ocean bottom electromagnetic meter (OBEM): To measure electromagnetic fields.
- Ocean bottom differential pressure gauge (DPG): To measure pressure changes.
- Ocean bottom gravity meter (OBG): To measure gravity.
- Tsunami pressure gauge: To measure tsunami pressure.
- ADCP (Acoustic Doppler Current Profiler): To measure water currents.
- Transmissometer: To measure light transmission.
- Gamma ray spectrometer: To measure gamma ray intensity.

Data from the observatory is transmitted to a land station on Hatsushima Island via an electro-optical cable, and some data is also sent to the JAMSTEC [18].

The prototype detector will be transported by ship from the JAMSTEC HONU in Yokosuka city and submerged in the sea for about 3 months. The installation period is determined by the available ship time. Application to use the research vessel to transport the prototype and deploy to the sea is being made.

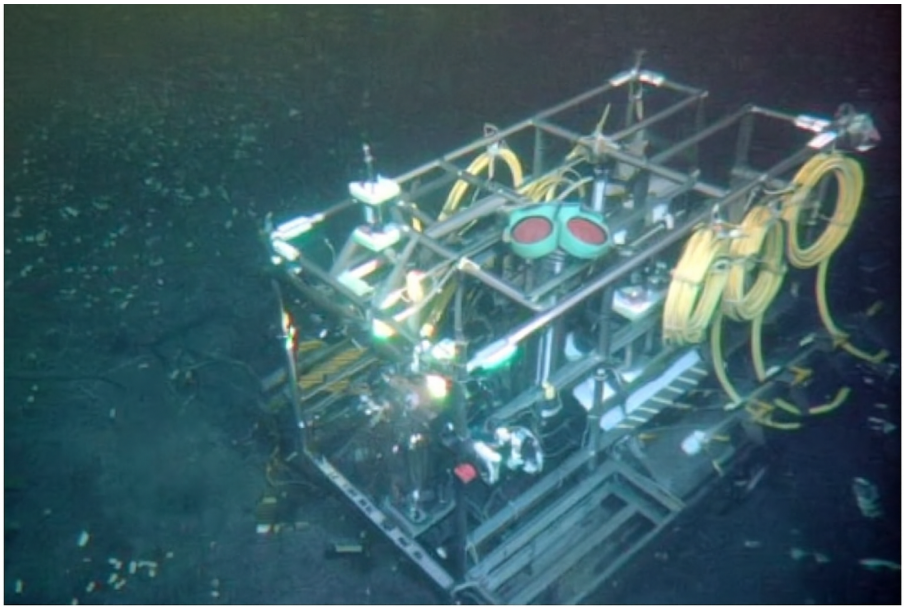

Figure 5.7: Cabled observatory off Hatsushima island

Chapter 6

Response and Optical performance of prototype detector

Although the main aim of an ocean based neutrino detector is to detect a a significant fraction of neutrinos originating from the mantle, the size of this prototype detector is too small to detect any neutrinos from natural sources.

The primary motivation behind the prototype is not neutrino detection itself but rather to evaluate the detector's performance, stability, and operational validation in the marine environment. To regularly monitor the detector response, a gamma calibration source will be used to give a constant output from the detector.

Response of a detector depends upon its configuration and the type of radiation incident on it. The detection medium in the prototype is LAB based organic liquid scintillator. Since the prototype will be surrounded by water, and is contained inside a steel vessel, gamma sources will be the good calibration sources due to their good penetration ability. However, organic scintillators owing to their low atomic number Z, have low cross sections in full energy photopeak, and their energy spectrum is mainly due to Compton scattered electrons. Hence, organic liquid scintillators have poor energy resolution for gamma radiation [25].

The energy deposited by the incident radiation causes scintillation in the LS and optical photons are produced which then reach the photocathode surface of PMTs and electric signals are produced. The detector responds to the energy deposit with these electrical signals.

6.1 Gamma ray interaction in the prototype detector

Compton scattering is the main gamma interaction process for gammas with liquid scintillator.

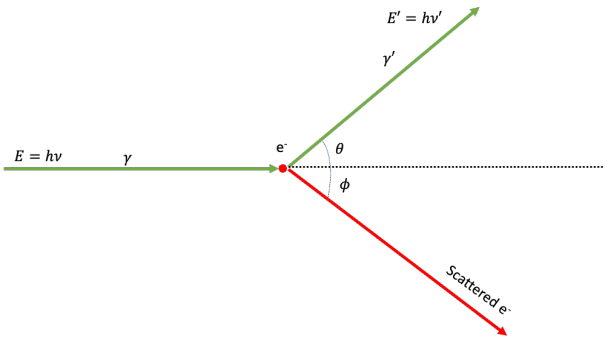

Figure 6.1: Compton Scattering Process

Energy of the scattered photon is given by :

$$E' = \frac{E}{1 + \alpha(1 - cos\theta)} \tag{6.1}$$

where $\alpha = E/m_0c^2$.

Energy of the recoil Compton electron is

$$T_c = \frac{\alpha E(1 - cos\theta)}{1 + \alpha(1 - cos\theta)} \tag{6.2}$$

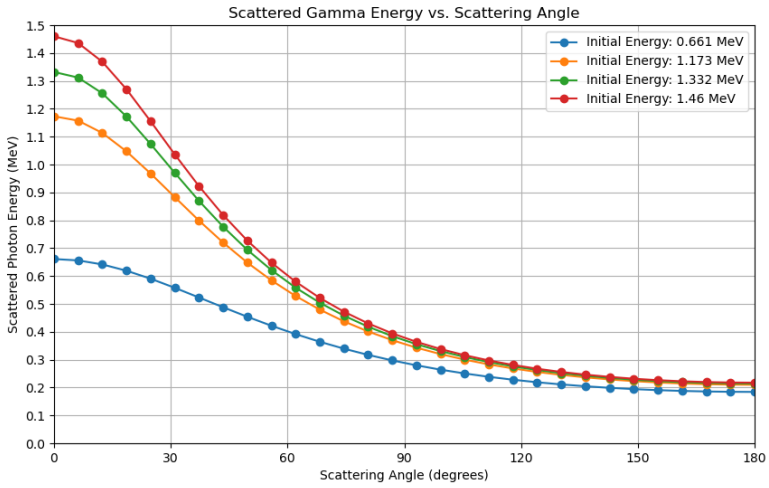

(a) Variation of energy of Compton scattered gamma with scattering angle θ

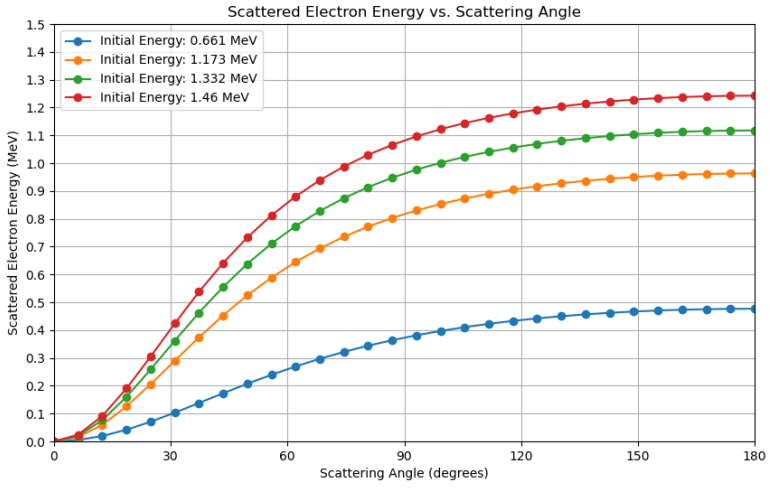

(b) Variation of energy of Compton scattered electron with scattering angle θ

Figure 6.2: Compton scattering energy transfer between gamma and electrons with scattering angle

Scattering angle $\theta = 180°$ represents the maximum energy T_{cm} that can be transferred in Compton scattering to the electron. This energy represents the Compton edge in Compton spectrum of gamma interactions in scintillators.

Source of gamma	Gamma energy (MeV)	E_{max} Compton scattered e^- (MeV)
Cs137 - calibration source	0.661	0.477
Co60 - calibration source	1.173	0.963
Co60 - calibration source	1.332	1.1176
K40 - from seawater	1.46	1.246

Table 6.1: Compton edge energies of some gamma calibration sources

6.1.1 Interaction cross section

In the case of liquid scintillators, because of their low density (about 0.87 g/cc) and low atomic number Z of the constituent elements, organic LS have much lower gamma-ray absorption coefficients than inorganic scintillators like NaI, CsI, etc.

We can calculate the Compton cross section using the Klein-Nishina formula:

$$\frac{\mathrm{d}\sigma}{\mathrm{d}\Omega} = \frac{\hbar^2\alpha^2}{2m_e^2c^2}\left(\frac{\lambda}{\lambda'}\right)^2\left[\frac{\lambda}{\lambda'} + \frac{\lambda'}{\lambda} - \sin^2\theta\right], \tag{6.3}$$

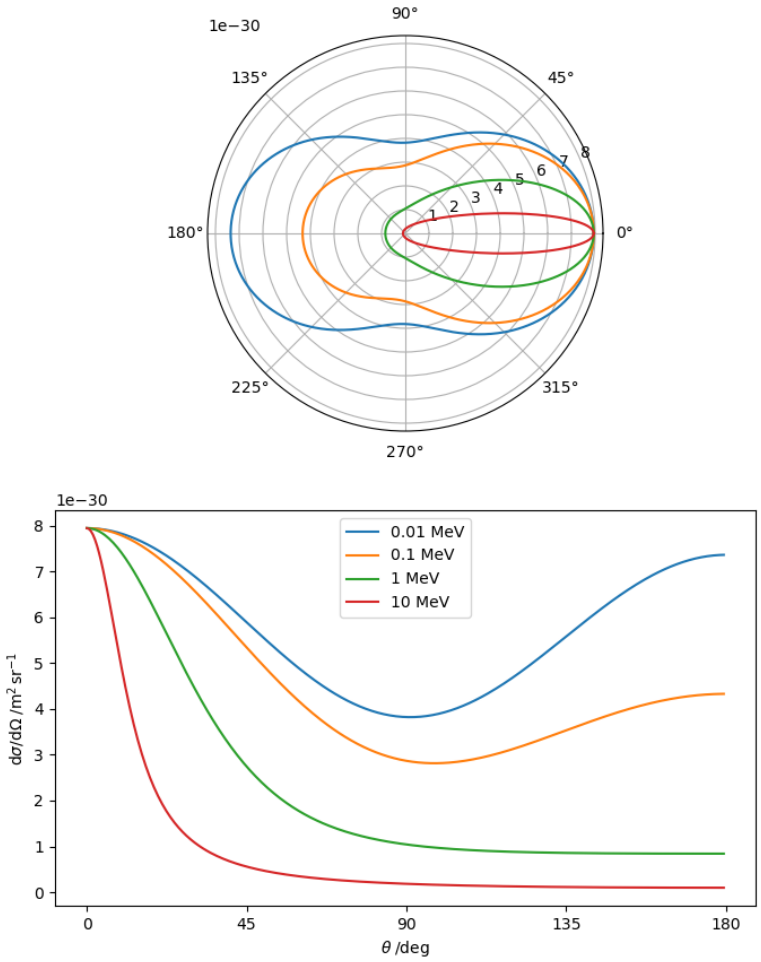

Figure 6.3: Angular dependence of the differential cross section at different incoming photon energies. At low energies, forward and back-scattering are equally likely (blue line: 10 keV); at high energies, forward scattering dominates (red line: 10 MeV)

6.1.2 Attenuation of gamma

Transmission probability of a gamma ray of energy E in a material can be calculated as:

$$P = e^{-\mu x} \tag{6.4}$$

μ is the attenuation coefficient, which depends on the energy E of gamma, interaction cross section, and density of material.

Stainless steel vessel strongly attenuates the gamma radiation. In case of 661 keV gamma, the transmission probability through 1 cm of steel is about 56%

$$\mu = 0.5835 \text{ cm}^{-1}$$

$$P = e^{-0.5835 \times 1} = 0.56$$

So the intensity of the radiation is significantly reduced before it enters the liquid scintillator.

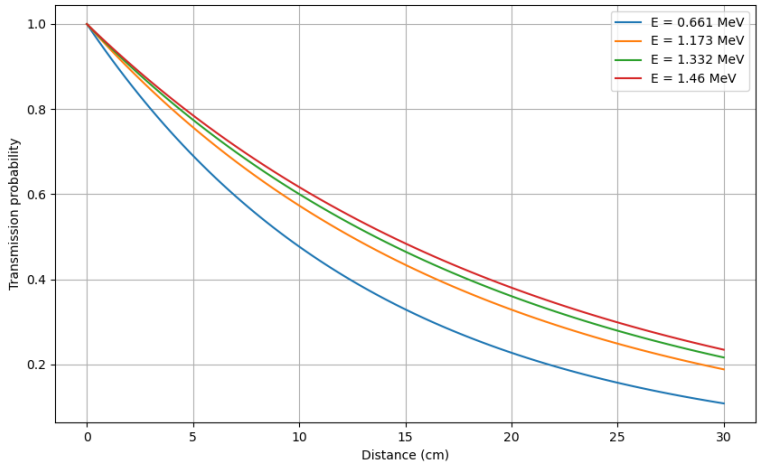

Figure 6.4: Transmission probability vs distance for gamma radiation in liquid scintillator

6.2 Energy deposition by gamma in prototype detector

In order to account for the complex mechanisms of energy deposition by gamma in the detector which includes interaction with the stainless steel vessel, a Monte Carlo simulation using the Geant4 toolkit [26] was performed. Geant4 version 11.0.4 was employed with a physics list based on hadronic interaction class FTFP_BERT and electromagnetic physics class G4EmStandardPhysics to account for the Compton scattering process.

The geometry of the detector is defined as follows (fig 6.5, table 6.2). All calibration sources from table 6.1 are placed on top of the stainless steel vessel.

Component	**Shape**	**Dimensions (cm)**	**Density** (g/cm^3)	**Material**
Stainless steel vessel	Cylinder	radius = 14, length = 20	7.938	`G4_STAINLESS_STEEL`
liquid scintillator	Cylinder	radius = 13, length = 20	0.856	`LAB`

Table 6.2: Geometrical and material properties of detector components.

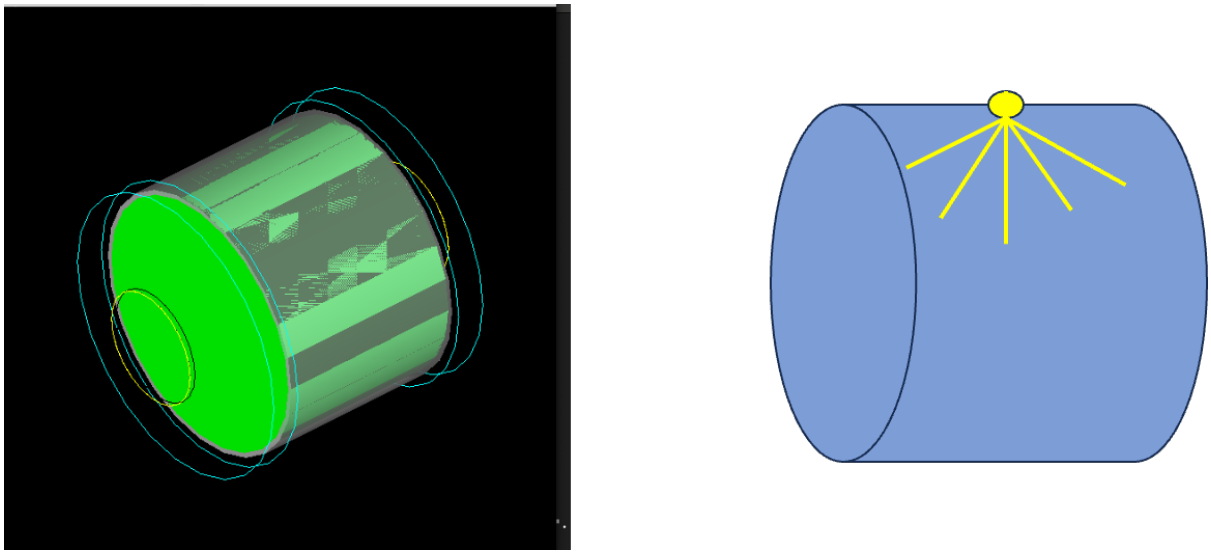

Figure 6.5: Setup definition in Geant4 and Placement of calibration sources

The simulation modeled the gamma-ray interactions in the detector and tracked the secondary electrons to get the energy deposition (fig 6.6).

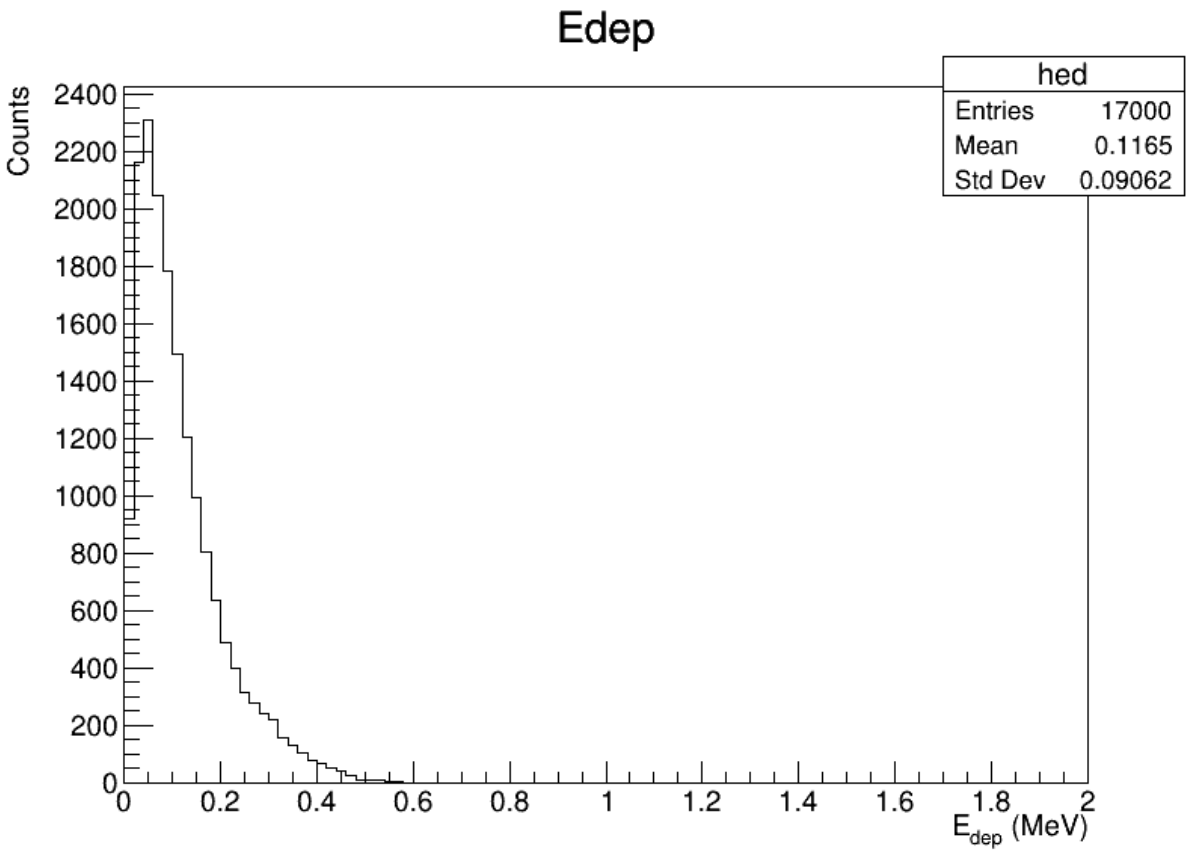

Figure 6.6: Simulated energy deposition from a Cs137 source in detector

6.3 Light Collection efficiency

Light Collection Efficiency (LCE) is an important factor in describing the optical performance of a detector. It is given by

$$\text{Light collection efficiency} = \frac{\text{Number of photons reaching at PMTs}}{\text{total number of photons generated}} \tag{6.5}$$

We can analytically derive it using solid angle calculation.

Theoretical Calculation

Assume an event at the center of the LS volume, scintillation light will be emitted isotropically. Amount of light reaching the PMT surface can be calculated by the solid angle subtended by the PMT surface at the center of LS volume (fig 6.7).

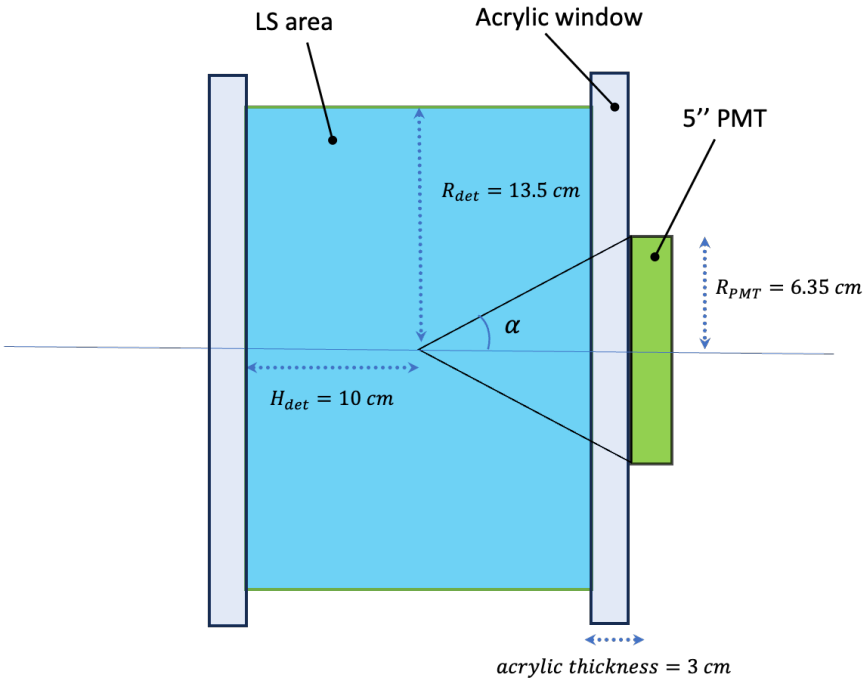

Figure 6.7: Detector setup diagram to calculate Light Collection Efficiency

Solid angle subtended by the PMT surface at the center is given as:

$$\Omega = 2\pi(1 - cos(\alpha)) \tag{6.6}$$

where α is called the half angle and is given as

$$\alpha = \tan^{-1}\left(\frac{\text{Radius of PMT}}{\text{distance from center}}\right) \tag{6.7}$$

LCE can be given by the ratio of Ω and total solid angle 4π.

$$LCE = \frac{\Omega}{4\pi} \tag{6.8}$$

If we use a 5 inches head on PMTs, light collection efficiency is calculated to be about 5%.

6.3.1 Optical Performance Comparison with D-Egg Parameters

The optical simulations presented in this thesis for the prototype detector (e.g., Fig. 6.13) have been performed assuming conventional spherical glass shields housing the PMTs. This geometry matches the

current mechanical design of the stainless steel tank and complies with the maximum hanging weight constraints for deployment from the research vessel.

For reference, the potential impact of using next-generation D-Egg optical modules, developed for the IceCube-Gen2 experiment, can be estimated from analytical calculations of light collection efficiency. The D-Egg uses two 8-inch high quantum efficiency PMTs enclosed in an ellipsoidal pressure-resistant glass housing, with integrated electronics and environmental monitoring sensors. Based on solid angle coverage from the larger photocathode area, the analytical estimate indicates a light collection efficiency of approximately 11 %, compared to about 5 % for the current spherical shield configuration. This gain would be further enhanced by the higher quantum efficiency of D-Egg PMTs.

It is emphasized that this estimate is not the result of a full D-Egg geometry simulation; the current optical simulations in this work retain the spherical shield geometry. The D-Egg performance is therefore presented only as a reference value, with full mechanical and electronic integration remaining a future design consideration (see Section 5.3.1).

6.4 Photon Simulation in Geant4

To evaluate the photoelectron response of the prototype detector and its intrinsic resolution, detailed optical photon simulations were carried out using the Geant4 toolkit. The simulations incorporate wavelength-dependent optical properties of the materials and track scintillation photons from their creation to their potential detection at the photocathodes of photomultiplier tubes (PMTs). All relevant processes: refraction, reflection, absorption, and quantum efficiency were modeled using the *G4OpticalPhysics* module with the *glisur* surface model for boundary interactions.

6.4.1 Laboratory Setup and Validation of Simulation Parameters

A simplified geometry was simulated to match the laboratory experiment (fig 6.8). The detector consisted of a cylindrical stainless steel vessel filled with LAB+PPO liquid scintillator, sealed on both ends with 3 cm thick acrylic windows. Two 5-inch head-on PMTs (Hamamatsu H6527) were mounted on either end of the vessel, without any glass shields or surrounding water.

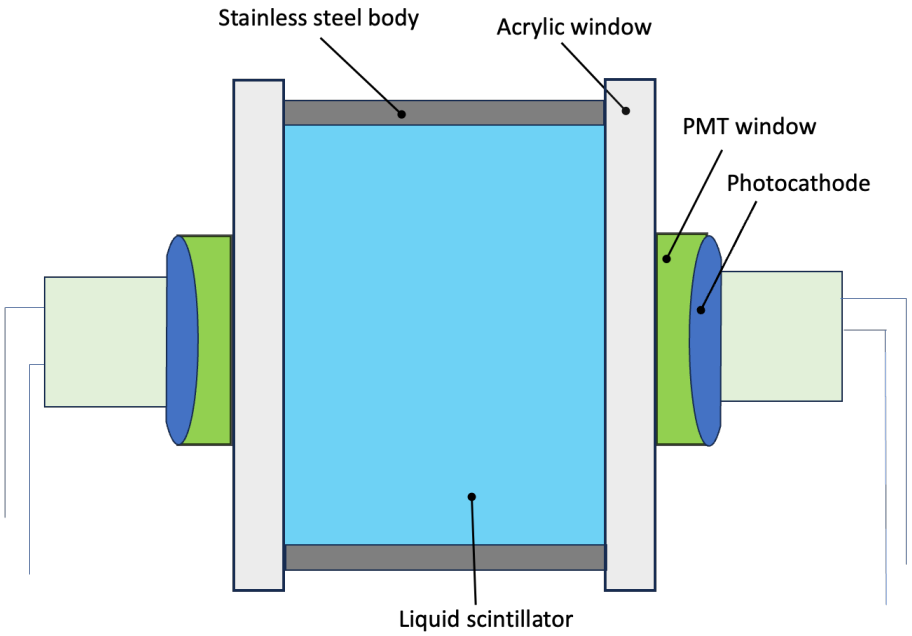

Figure 6.8: Detector setup in the laboratory, with two 5 inches head on PMTs mounted on the both ends of detector. 3 cm acrylic is used to separate scintillator volume from the PMTs. Stainless steel vessel of 1 cm thickness is used to contain the scintillator

A ^{137}Cs source was positioned outside the steel vessel to replicate the experimental calibration setup.

Gammas were simulated as primary particles and their energy deposition in the scintillator was modeled via Compton scattering. Scintillation photons were generated using a yield of 8000 photons/MeV and tracked to the PMTs. Conversion of photon to photoelectron was implemented using a wavelength-dependent quantum efficiency curve with a peak of ∼25% (fig 6.9).

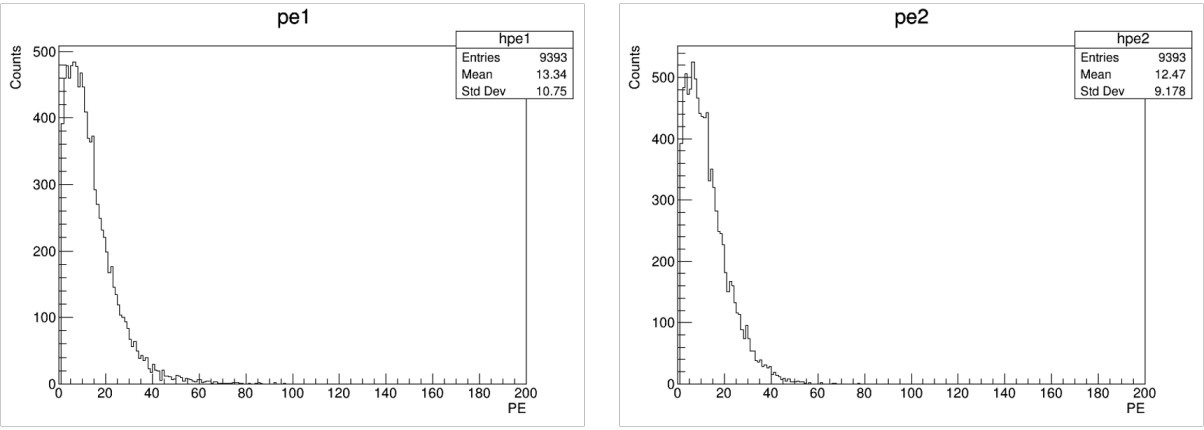

Figure 6.9: Simulated Photoelectron distribution in the 2 PMTs

Intrinsic Resolution

The intrinsic energy resolution is the theoretical minimum width of the detector's energy response arising purely from photon counting statistics, optical photon transport, and photodetector quantum efficiency for a specific detector geometry. It is a property of the detector design itself and does not include contributions from electronics, PMT gain variations, source position effects, or incomplete energy deposition from external gamma sources.

For the prototype detector, the intrinsic resolution depends on the geometry and optical configuration such as scintillator volume, optical boundary conditions, reflective surfaces, PMT size and placement and light yield of the scintillator. Any change in these parameters, for example switching from 5-inch to 8-inch PMTs or adding optical interfaces like glass shields, alters the number of photoelectrons detected per unit energy and therefore changes the intrinsic resolution.

In a scintillator, light production is ultimately caused by energetic electrons rather than gamma rays themselves. Gamma interactions such as Compton scattering or the photoelectric effect first transfer energy to electrons, which then lose energy in the scintillator medium through excitation and ionization, which eventually results iin the production of scintillation photons. This is why, for evaluating the intrinsic resolution, monoenergetic electrons are generated at the center of the liquid scintillator volume in the simulation. Electrons deposit their full energy locally, ensuring that the light yield reflects only the scintillation process and the detector's optical collection efficiency, without being influenced by position dependent attenuation or the partial energy deposition that occurs in gamma interactions.

Using electrons also allows the results to be expressed directly in the unit of MeV electron-equivalent (MeVee), which is standard in scintillator calibration. The MeVee scale is defined so that 1 MeV deposited by an electron corresponds to 1 MeVee of light output. Different particles produce different light yields for the same deposited energy due to quenching effects, but by using electrons the simulation directly corresponds to the calibration baseline, making the results physically meaningful and comparable to measurements.

With this approach, the resulting photoelectron distribution in the simulation reflects only the fundamental photon statistics limit for that detector configuration. The intrinsic resolution is then obtained from the relative width (σ/E) of this distribution as a function of electron energy. This provides a source independent performance baseline for comparing detector designs. Also, by comparing intrinsic resolution from simulation with measured resolution from calibration data, one can identify how much of the measured width comes from unavoidable statistical broadening and how much comes from other degradations due to electronics, environmental conditions, or incomplete light collection.

$$\frac{\sigma}{E} = \frac{\sigma_{\text{p.e.}}}{\mu_{\text{p.e.}}} \tag{6.9}$$

$\mu_{\text{p.e.}}$ and $\sigma_{\text{p.e.}}$ are the mean and standard deviation of the photoelectron distribution, respectively. This corresponds to an ideal resolution determined purely by photon-counting statistics.

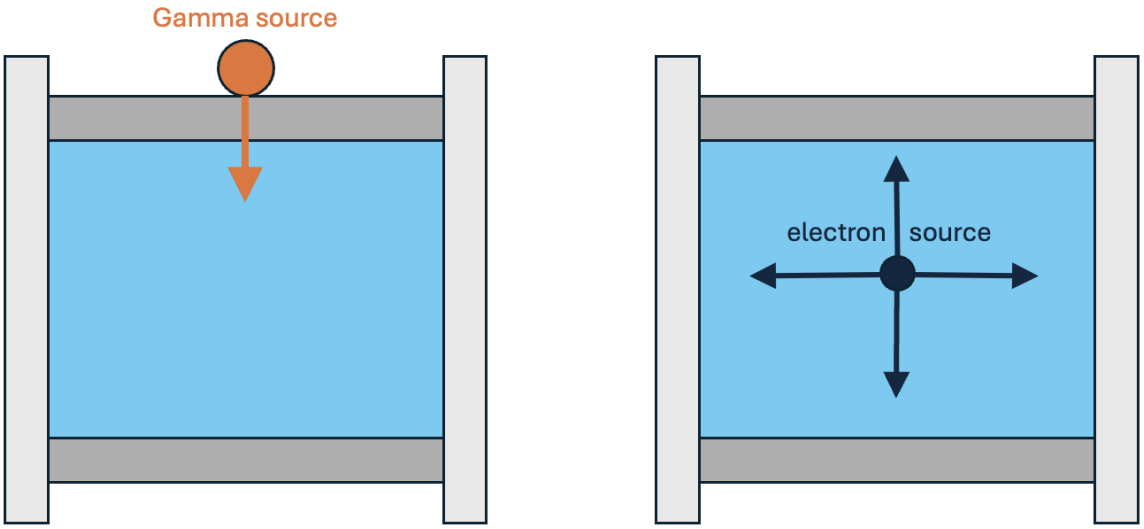

Figure 6.10: Left: Laboratory configuration used for simulation–experiment comparison, with the gamma calibration source (Cs-137) placed outside the stainless steel vessel, above the detector. Gammas interact mainly via Compton scattering, producing recoil electrons that generate scintillation light. Right: Configuration used for intrinsic resolution evaluation, with a monoenergetic electron generated at the center of the liquid scintillator volume. This setup ensures full local energy deposition in the scintillator and a direct light output in MeV electron-equivalent (MeVee), removing geometric and attenuation effects present in the gamma setup.

For the detector configuration with 5-inch PMTs as used in the laboratory (fig 6.8), the intrinsic resolution was found to be about $23.4/\sqrt{E}$ %.

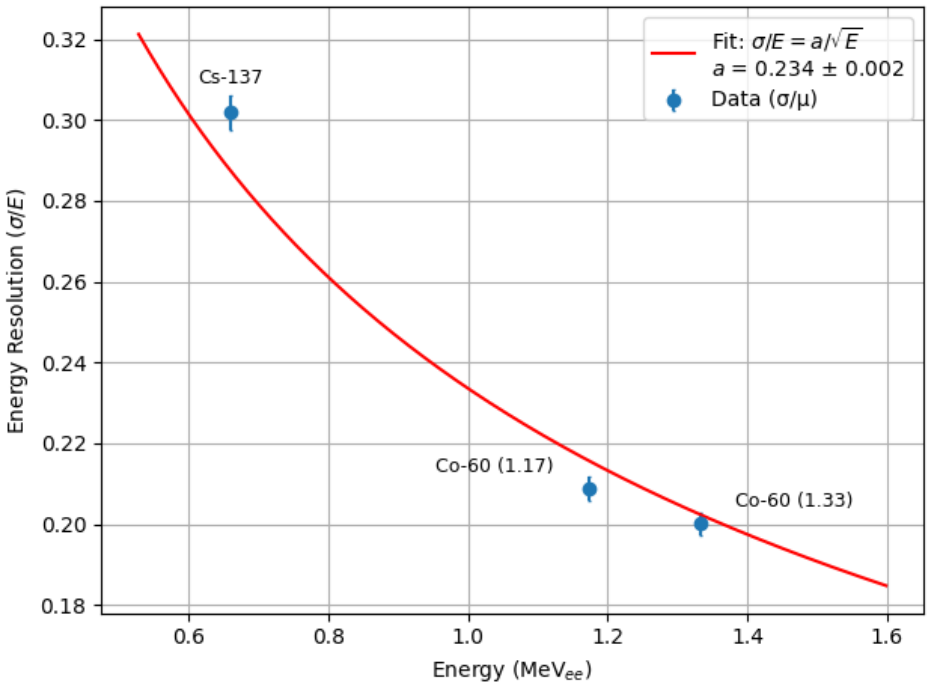

Figure 6.11: Intrinsic resolution of the detector for configuration as shown in fig 6.8

In this study, the photomultiplier-tube (PMT) gain and the scintillator light yield were treated as free parameters and adjusted by matching the simulated photoelectron spectrum to the experimentally measured charge distribution. The resulting best-fit values approximately 1×10^7 for the PMT gain and about 8,000 photons/MeV for the light yield are consistent with the manufacturer's specifications and values reported in the literature. Remaining discrepancies between simulation and experiment are ascribed to idealizations in the Monte Carlo model and to the fact that only the intrinsic resolution (defined by photon-counting statistics) was applied. As explained earlier, this intrinsic resolution omits additional broadening effects from electronic noise and other instrumental contributions present in the full detector system.

6.4.2 Calibration of PMT Gain and Scintillator Light Yield

In this work, the PMT gain and scintillator light yield were determined via an iterative tuning procedure. First, a large Monte Carlo dataset of single electron events in the liquid scintillator volume was generated, propagating optical photons through all detector interfaces and surfaces. Each optical photon reaching a PMT photocathode was converted into a simulated photoelectron under the quantum efficiency of PMTs used in experiment. Next, the simulated photoelectron counts were mapped to an expected charge spectrum by applying trial values for the PMT gain G and light yield Y.

The parameters G and Y were then adjusted manually, comparing the simulated charge histogram to the experimentally measured spectrum from a standard Cs137 gamma ray source. The best-match values were found to be

$$G_{\text{best}} \approx 1.0 \times 10^7, \qquad Y_{\text{best}} \approx 8{,}000 \text{ photons/MeV}.$$

These results lie within the manufacturer's ± 10 % tolerance for the PMT gain and agree with typical light yield values for linear alkylbenzene based scintillators reported in the literature.

Although the simulated peak position and width agree well with experiment, discrepancies remain in the high-charge tails. These are attributed to:

1. **Model Idealizations:** Simplifications such as uniform photocathode response, perfect optical coupling, and ideal reflectivity of vessel surfaces omit small but non-negligible real-world effects.
2. **Intrinsic Resolution Only:** The simulated energy resolution includes only the intrinsic photon-counting (Poisson) component,
$$\frac{\sigma_E}{E} = \frac{1}{\sqrt{N_{\text{pe}}}}$$
and excludes additional broadening from electronic noise, baseline fluctuations, and PMT transit-time spread.

For future refinement, a composite resolution model may be introduced:

$$\left(\frac{\sigma_E}{E}\right)^2 = \frac{1}{N_{\text{pe}}} + \left(\frac{\sigma_{\text{elec}}}{E}\right)^2 + \left(\frac{\sigma_{\text{tts}}}{E}\right)^2,$$

where σ_{elec} denotes the electronic noise contribution and σ_{tts} the PMT transit-time jitter. However, isolating the intrinsic term here provided a clear benchmark against manufacturer data and literature without introducing extra free parameters.

Another way of extracting resolution from the experimental data is the convolution method. The convolution method is a common approach to extract the energy resolution of a liquid scintillator detector by directly comparing experimental spectra with simulated or analytically expected distributions. In this technique, a high-statistics Monte Carlo simulation is generated for the relevant source and detector geometry, producing an "ideal" energy spectrum without resolution smearing. This ideal spectrum is then convolved with a Gaussian response function whose width is parameterized as

$$\sigma(E) = \frac{a}{\sqrt{E}},$$

where a is the resolution parameter and E is the deposited energy, usually expressed in MeV electron equivalent (MeVee). By varying a and performing a fit to the experimental spectrum, the best-fit Gaussian width reproduces the observed peak broadening, thereby providing a quantitative measure of

the detector's energy resolution. This method naturally incorporates the spectral shape from physical processes in the scintillator (example, Compton scattering for gammas) and isolates the contribution of statistical photon-counting fluctuations and optical transport to the measured resolution.

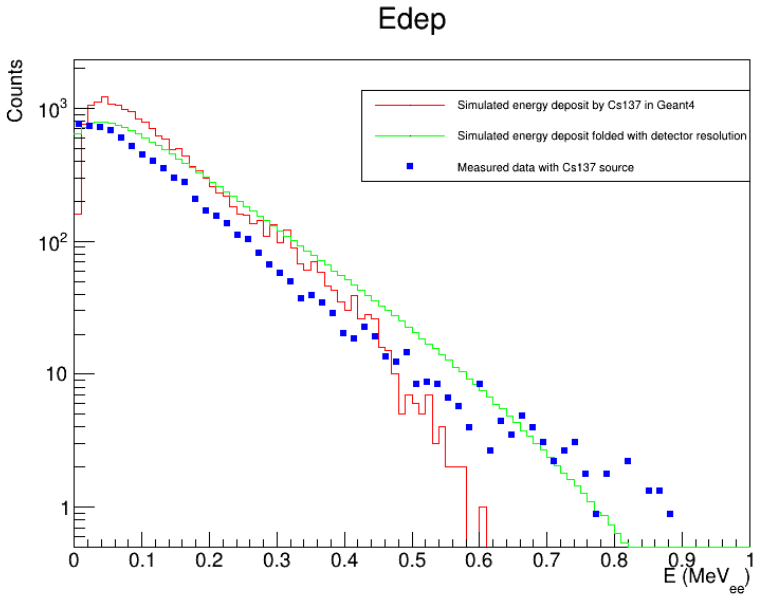

Figure 6.12: Comparison of simulated and experimental response. Red histogram shows the simulated energy deposit without any resolution effect. Green histogram shows the folded energy deposition spectrum with the intrinsic resolution as determined (fig 6.11). Blue dots represent the measured data form experiment.

6.4.3 Simulation of Marine Environment Configuration

After validation, the simulation was updated to reflect the marine environment configuration. In the marine setting, that is the actual deployment setting of the prototype, bigger PMTs in glass shells will be used. The entire detector would be submerged in seawater. Moreover, the temperature of the environment will be lower about 4°C. Due to the lower temperature, the optical properties of the liquid scintillator will be changed. An increased light output of about 10% has been observed for linear alkylbenzene liquid scintillator. All of these modifications are included in the simulation for marine environment/deployment configuration:

- Replacement of 5-inch PMTs with 8-inch PMTs.
- Addition of pressure-resistant glass shields enclosing the PMTs.
- Introduction of optical grease layers between PMT windows and glass shields.
- Immersion of the entire detector in seawater.
- Increase in scintillator light yield by 10% to model low-temperature operation (∼4°C).

At each interface between different detector media, specifically between the liquid scintillator (LS) and stainless steel, LS and acrylic, acrylic and glass, glass and optical grease, and optical grease and the PMT window — appropriate optical surface definitions were implemented in the Geant4 simulation. These boundaries were assigned to either dielectric–dielectric or dielectric–metal types, depending on the physical nature of the two adjoining materials. For dielectric–dielectric interfaces (e.g., LS–acrylic, acrylic–glass, glass–grease, and grease–PMT window), the simulation accounted for photon refraction and reflection using Fresnel equations, governed by the wavelength dependent refractive indices of each material.

In the case of the LS–stainless steel boundary, a dielectric–metal interface was defined to incorporate reflective behavior from the polished steel surface, which influences the probability of photons being redirected toward the PMTs. In addition, wavelength-dependent optical properties such as refractive index and absorption length, and.

This careful definition of boundary processes ensured realistic modeling of photon transport, including effects such as total internal reflection, partial transmission, and absorption losses, which are critical for accurately predicting the detector's light collection efficiency and photoelectron yield.

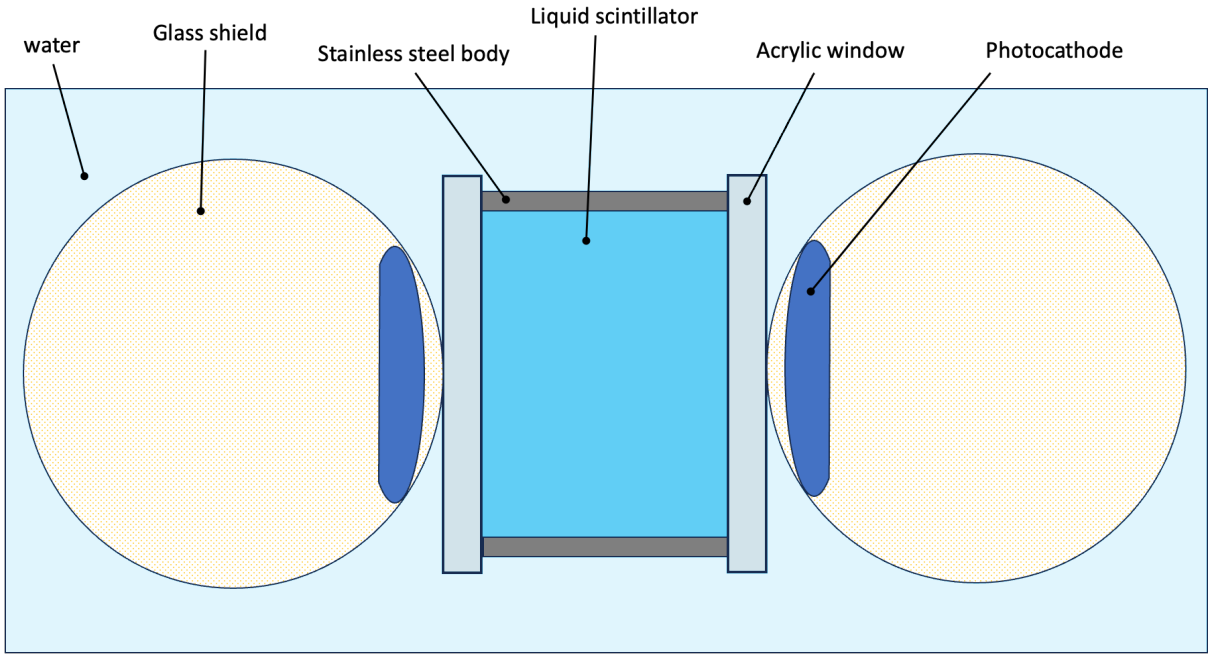

Figure 6.13: Detector setup as expected in the sea. PMTs are enclosed in glass shields and entire setup is submerged in water

Electron events with energies of 0.661 MeV, 1.17 MeV, and 1.33 MeV were simulated by generating monoenergetic electrons at the center of the liquid scintillator. This approach directly evaluates the detector's intrinsic resolution, the limit set by photon-counting statistics, optical transport, and PMT efficiency while avoiding attenuation and partial energy deposition effects from gamma interactions as done for the laboratory setup. Since scintillation light is produced by electrons and results are expressed in MeV electron-equivalent (MeVee), this method ensures direct correspondence with the standard calibration scale. The photoelectron spectra were Gaussian, and the intrinsic resolution from equation 6.9 showed that improved geometry and optical conditions in the sea setup increased photoelectron yield by about 75 % over the laboratory case, resulting in a resolution improvement to:

$$\frac{\sigma}{E} \approx \frac{13.3\%}{\sqrt{E\ (\text{MeV})}} \tag{6.10}$$

This represents a significant enhancement in performance attributable to increased light yield and more efficient photon detection.

6.4.4 Summary

The Geant4 simulations provided a quantitative evaluation of the intrinsic energy resolution of the prototype detector under two configurations: a simplified laboratory setup and a fully instrumented marine environment. The main findings are:

- The simulation reproduced the trend of experimental ^{137}Cs response when gain and light yield were tuned.
- The intrinsic resolution derived from simulations is idealized, based solely on photoelectron fluctuations.
- The simulated marine configuration exhibits significantly better performance due to colder scintillator, larger PMTs, and enhanced photon transmission.

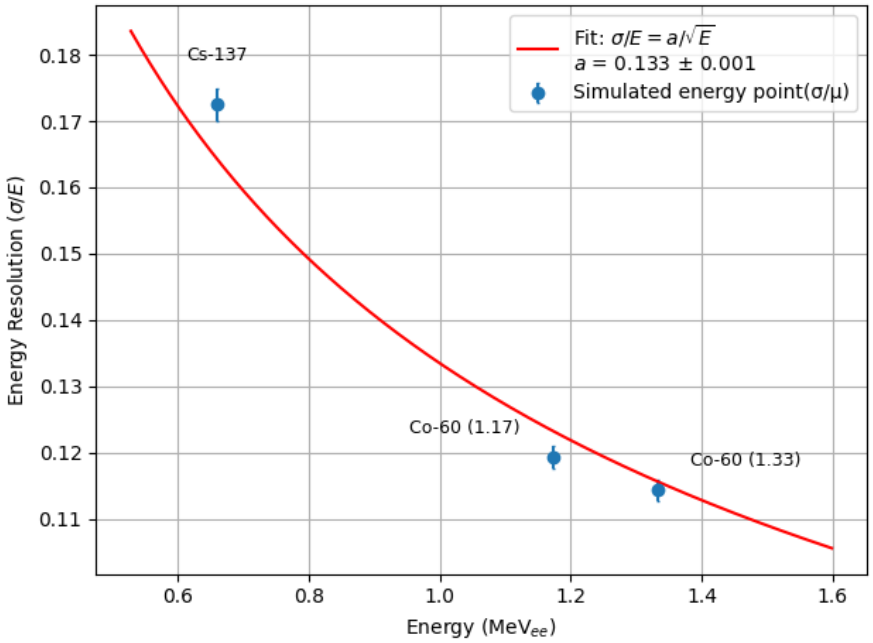

Figure 6.14: Intrinsic resolution for the detector as per the setup planned for the deployment in the sea (fig 6.13)

These simulations establish a predictive baseline for interpreting data from the prototype once deployed in the sea and will support future calibration and energy reconstruction efforts.

Chapter 7

Environmental radiation and other background for prototype detector

In this chapter, we discuss the presence of external and environmental radioactivity present around the prototype detector in marine environment, model it using simulations and evaluate the detector's response to it.

This helps to create a baseline to monitor the detector performance over time. Any possible contamination or unusual activity can be easily separated from background signals. The baseline also supports accurate data analysis once the detector is deployed.

7.1 Radioactivity in the sea

Like land, oceans have environmental radioactivity. Although the oceans are not in secular equilibrium.

Radioactivity in the marine environment arises from naturally occurring isotopes, primarily potassium-40 (K-40), uranium-238 (U-238), and thorium-232 (Th-232), along with their decay products. Alpha particles due to their large size and charge, get effectively attenuated by seawater. Beta radiation from the above considered radioisotopes also do not possess enough energy to reach the detector. Hence, we will be neglecting these radiation in these simulations. But the gamma radiation can still reach the detector region and deposit a fraction of their energy. The most significant gamma radiation from sea originates from K-40 (1.46 MeV), and high-energy gammas such as the 2.620 MeV from Tl-208 in the Th series and the 1.760 MeV from Bi-214 in the U series. The distribution of these isotopes differs between sediments and seawater due to differences in solubility: uranium and potassium are soluble and relatively mobile in seawater, whereas thorium is not and instead accumulates in sediments. For the prototype detector, local seafloor radioactivity is a key background source. In the absence of site-specific measurements, this study assumes global average concentrations for coastal marine sediments: uranium typically ranges from 2–12 ppm (often 3–6 ppm) [27, 28, 29], thorium ranges from <1 to >20 ppm depending on sediment type (average 10 ppm in deep-sea sediments) [30, 31], and potassium averages about 18,500 ppm [32]. In seawater, due to the lack of secular equilibrium caused by differential solubility—uranium is partially soluble while thorium is not—thorium and the subsequent daughter isotopes are neglected as radiological contributors.

However, potassium remains significant due to its high solubility. Potassium has a radioisotope - Potassium 40 which is a major source of natural radioactivity in the entire Earth. It makes upto 0.012% of natural potassium. The global average of potassium concentration in seawater is fairly certain - 399 ppm [33]. Although K40 decays through 4 channels, the following two decay channels contribute to the radioactivity in the sea.

$$\begin{array}{rcll} {}^{40}K & \rightarrow & {}^{40}Ca + e^- + \overline{\nu_e} & (BR = 89.3\%) \\ {}^{40}K + e^- & \rightarrow & {}^{40}Ar + \nu_e + \gamma & (BR = 10.7\%) \end{array} \tag{7.1}$$

The electrons produced in $\beta-$ decay are neglected in this study due to the low attenuation length of

electrons in water. However, the gamma produced in the electron capture has a signature energy of 1.46 MeV, can travel centimeters in water and create potential noise in the detector.

Radioisotope	Concentration (ppm)	sediment / seawater
U238	3	in sediments
Th232	10	in sediments
K40	2.2	in sediments
K40	0.0478	in seawater

Table 7.1: U238, Th232, K40 concentration in sea

7.2 Radiation from detector components

In addition to environmental sources, intrinsic radioactivity within detector construction materials contributes to the background signal. Key materials under consideration include the acrylic used for the viewports, the glass shields enclosing photomultiplier tubes (PMTs), and the stainless steel tank. These components may contain trace amounts of naturally occurring radioisotopes such as uranium (U), thorium (Th), and potassium (K), which emit gamma radiation through their decay chains. Furthermore, stainless steel often contains anthropogenic cobalt-60 (Co-60), a strong gamma emitter with characteristic lines at 1.17 MeV and 1.33 MeV, introduced either through neutron activation or contamination during manufacturing. To quantify these contributions, simulations are carried out assuming realistic concentrations of U, Th, and K in each material based on published assay results and material specifications. The resulting gamma emissions are tracked to evaluate their impact on the prototype detector's background, particularly in the sensitive liquid scintillator volume.

U-238	Th-232	K40
1.0×10^{-11} g/g	1.0×10^{-11} g/g	1.0×10^{-11} g/g

Table 7.2: Acrylic's radioactive content [21]

For the glass shield, given that the plan involves employing IceCube's PMT glass modules, it is assumed that the radioactive content of these modules is present.

U-238	Th-232	K40
5.20 Bq/kg	1.16 Bq/kg	1.0 Bq/kg

Table 7.3: Glass shield's radioactive content [22]

Stainless steel is chemically incompatible with elements like Uranium and Thorium, so they exist in very minute amount. Nevertheless, since stainless steel is in direct contact with liquid scintillator, its radioimpurity is considered in this study. For stainless steel typical values of radioactive content is used from the literature[34].

U-238	Th-232	K40	Co60
1.0 mBq/kg	1.0 mBq/kg	1.0 mBq/kg	19.0 mBq/kg

Table 7.4: Stainless steel's typical radioactive content

7.3 Modeling background radioactivity in Geant4

In this section, presence of radioactivity is modeled around the detector using Geant4 and the detector's response is analysed. Following approach is used:

1. Create a geometry of complete prototype detector in Geant4 with water as the surrounding volume, and a bottom surface volume of sediment
2. Distribute the gamma sources randomly around detector and in the components

3. Find if the gammas can deposit any energy in the liquid scintillator (LS) region
4. Using Geant4 score the energy deposit inside LS
5. From the activity of radioisotopes, calculate the rate of energy deposition in LS

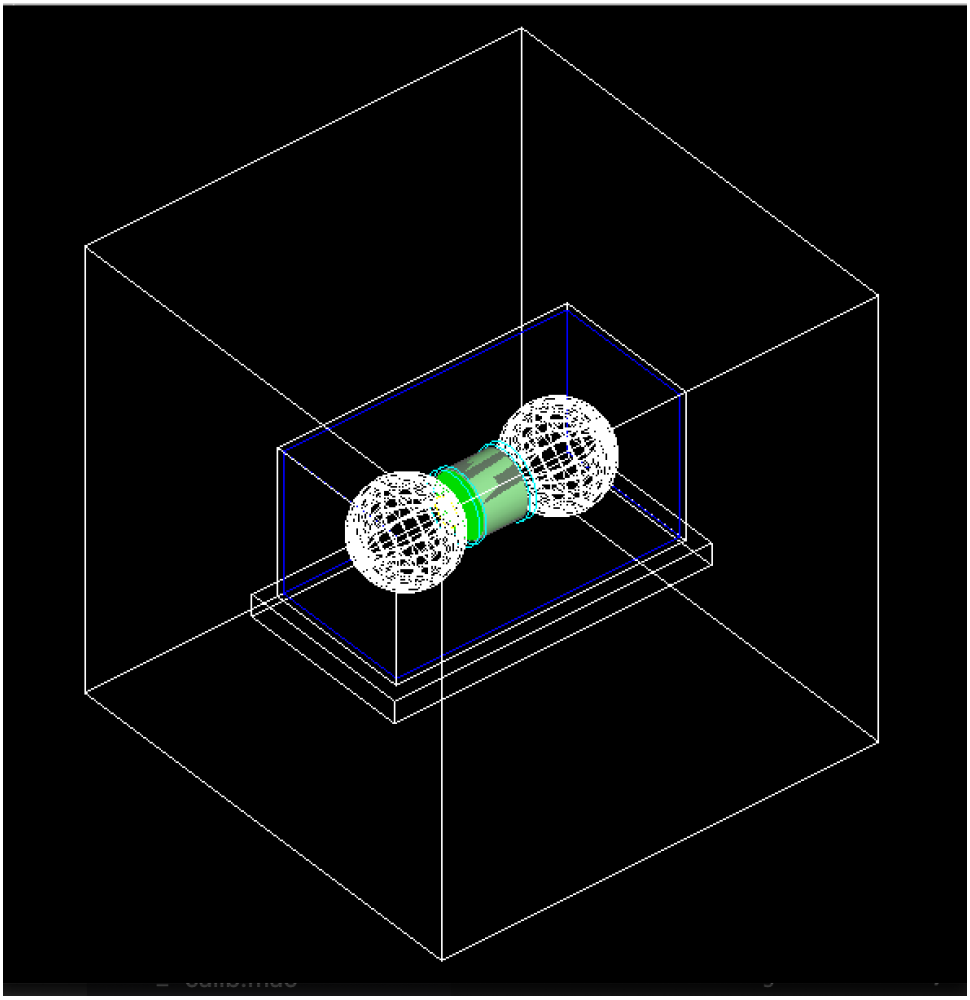

Figure 7.1: Geometry of prototype detector in marine setting with surrounding seawater and sediments on seafloor as designed in Geant4

7.4 Energy deposition and Event Rate Calculation

The *General Particle Source* class is employed to produce the primary events. In the case of K40 in seawater, monoenergetic gamma rays of 1.46 MeV are randomly distributed throughout the water volume to simulate the distribution of K40 in seawater. For radioisotopes in sediment and detector parts, gamma sources are also randomly spread within their respective volumes. When gammas enter the LS region, they undergo Compton scattering, with such scattering being modeled using the EmStandardPhysics option in Geant4.

To calculate the event rate from a radioisotope X, the following formula is used:

$$X_{\text{rate}} = \text{detection efficiency} \times X_{\text{mass}} \times X_a \tag{7.2}$$

where detection efficiency is the ratio of number of detected events and number of total simulated events.

$$\text{detection efficiency} = \frac{N_{\text{detected}}}{N_{\text{simulated}}} \tag{7.3}$$

X_{mass} is the total mass of radioisotope X given by multiplying the total mass of simulated volume with the concentration of X in that volume. The concentration is given in the tables (7.1, 7.2, 7.3, 7.4).

X_a is the specific activity of X given by, it gives the number of decays happening in per gram of the radioactive sample. It depends on decay constant of radioisotope λ, Avogadro's number N_A and molar mass of X - X_M.

$$X_a = \frac{\lambda * N_A}{X_M} \tag{7.4}$$

Comparing these background rates with calibration source Cs137's event rate, it looks like the background does not cause major interference. Here, we have assumed the source's activity as 2.5 MBq, which is a typical source used in laboratory experiments and is well within the activity limits specified by the Nuclear Regulations Authority.

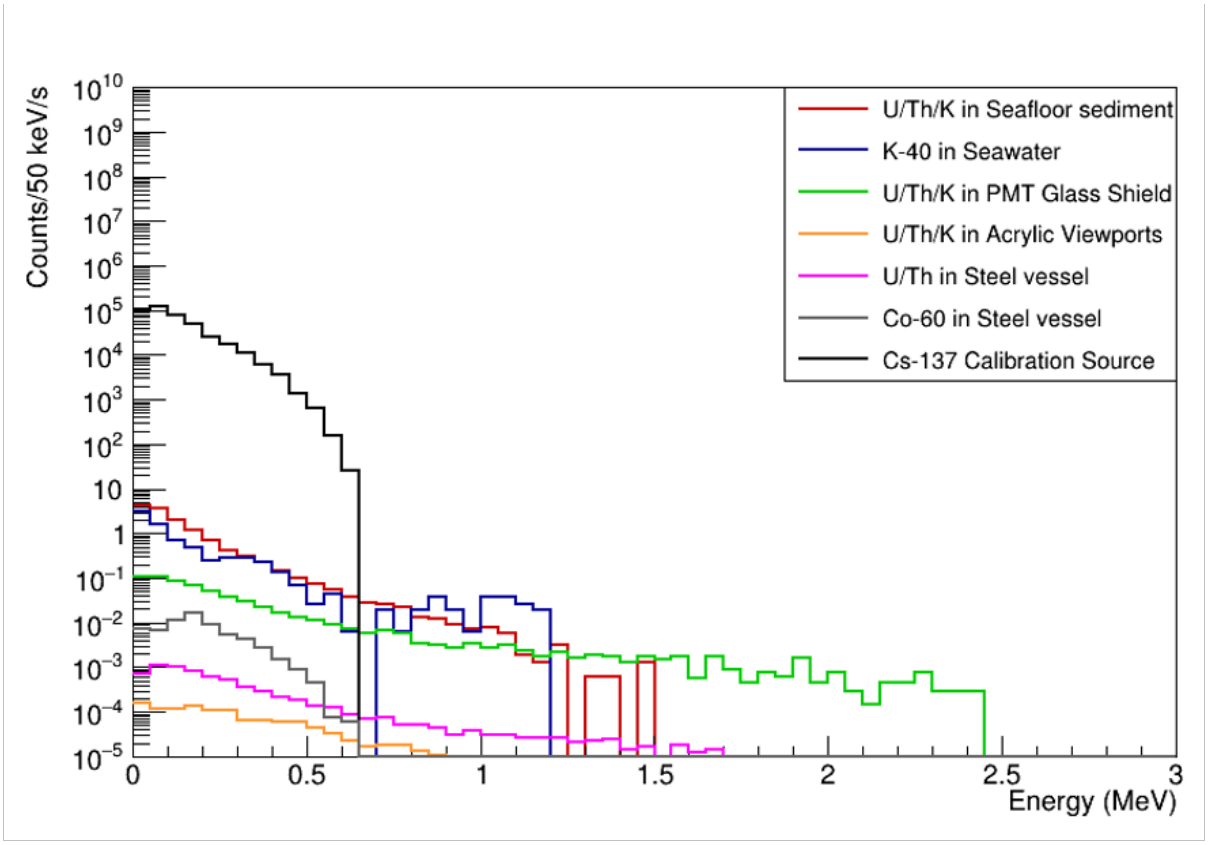

Figure 7.2: Background rate with calibration source's rate

7.4.1 Optimization of the calibration source activity

The background study presented in Fig. 7.2 demonstrates that the activity of the Cs-137 calibration source assumed in the baseline simulation (2.5 MBq) is much larger than necessary for reliable calibration of the prototype detector. The predicted energy deposition rate from natural environmental sources, including U/Th/K in sediments and seawater as well as radioactivity from detector components, is several orders of magnitude lower than the event rate induced by a 2.5 MBq Cs-137 source. Consequently, the signal from the source dominates the spectrum to such an extent that environmental backgrounds become negligible during a calibration run.

While such a high activity guarantees excellent statistics in a very short exposure time, it has two drawbacks for the planned three-month marine deployment: (i) the very high count rate may cause increased pile-up in the small-volume detector and potential dead-time in the data acquisition system; (ii) the unnecessarily intense source complicates handling and transport procedures, which must be performed under strict radiological safety requirements for deep-sea deployment.

Proposed activity range. From the simulated event rate shown in Fig. 7.2, it can be inferred that a two order of magnitude reduction in source activity would still provide a calibration spectrum that rises far above the background. For example, even a 25-30 kBq source produces a count rate approximately

100–1000 times greater than the combined background rate in the energy region around 0.66 MeV, ensuring a clean and distinct Compton edge and peak structure. Based on this consideration, it is proposed to optimize the source activity to a value in the range of 2×10^4 Bq to 3×10^4 Bq.

Quantitative reasoning for 20–30 kBq. The 2.5 MBq source simulated in this study produces an event rate that exceeds the combined background by 4-5 orders of magnitude across the full spectrum. Reducing the source activity by a factor of 100, to 25 kBq, brings the induced event rate down to about 10^3-10^4 events/s, which is still at least two orders of magnitude above the background while avoiding PMT saturation and dead-time. This activity range provides a comfortable margin: it ensures that the calibration spectrum remains clearly separated from the background while keeping the rate manageable. Activities lower than about 20 kBq would slow the acquisition to the point that several days of integration would be required, while activities higher than 30 kBq bring little benefit but reintroduce the operational difficulties associated with strong sources.

Impact on calibration. Reducing the activity by two orders of magnitude directly reduces the rate of recorded events by the same factor. As a result, the statistical precision achievable in a given period will decrease; however, this effect can be compensated for by extending the calibration acquisition period. For instance, if a 2.5 MBq source can produce a high-statistics spectrum in $\sim$10 seconds, a 25 kBq source will require approximately 1000 seconds of acquisition to achieve a comparable number of events. Given that the prototype detector will be continuously deployed on the seafloor for a period of three months, such extended acquisition times are entirely feasible and do not hinder the overall data-taking plan.

Advantages of a weaker source. The use of a lower-intensity calibration source offers many practical benefits:

- **Reduction of pile-up and dead-time:** A lower event rate avoids excessive coincidence pileup in the PMTs and reduces the risk of dead-time losses in the readout electronics.
- **Simplified handling:** A weaker source reduces radiological hazards during deployment and retrieval operations, and relaxes some of the procedural constraints on transport and storage.
- **Cleaner monitoring:** With the reduced activity, the signal-to-background ratio remains very high, while allowing the monitoring of slow temporal drifts in detector response with improved control over count rates.

The simulations confirm that such an optimization would not compromise the ability to monitor detector stability throughout the three-month deep-sea observation period.

Chapter 8

Optical Design Study of a Large-Size Detector

8.1 Introduction

The optical performance of large-volume liquid scintillator detectors is critical to achieving the sensitivity required for neutrino physics. In these detectors, scintillation light generated by particle interactions must traverse multiple material layers before reaching the photomultiplier tubes (PMTs) at the periphery. Attenuation, refraction, and absorption within each layer substantially impact photon survival and thus the overall detection efficiency.

An idealized *spherical shell* model is introduced as a conceptual tool to isolate the effect of layer thickness on light transmission. In this configuration, every photon emitted at the center travels radially through identical thicknesses of acrylic and buffer oil, such that the total transmission becomes an explicit function of these thicknesses alone. Under Beer–Lambert attenuation,

$$T(L, \lambda) = \exp\big[-L \,/\, \lambda_{\mathrm{abs}}(\lambda)\big], \tag{8.1}$$

the problem reduces to two independent variables, L_{acrylic} and L_{oil}, without angular path-length variations. By scanning $L_{\mathrm{acrylic}} = 5$–$30\,\mathrm{cm}$ and $L_{\mathrm{oil}} = 0.5$–$1.5\,\mathrm{m}$, the optimal thickness window for maximal photon survival is identified. Once these radial values are determined, they may be translated into any practical detector geometry -cylindrical, polygonal, or hybrid; while preserving the same optical budget.

8.2 Parametric Layer-Thickness Geometry

The detector model is based on this conceptual spherical-shell approach (Fig. 8.1). It comprises:

- A central liquid scintillator sphere of radius $R_{\mathrm{LS}} = 7\,\mathrm{m}$, fixed so as to hold 1.5kt of liquid scintillator;
- A concentric acrylic vessel of variable thickness L_{acrylic};
- An outer buffer-oil shell of variable thickness L_{oil};

Because every photon traverses exactly L_{acrylic} of acrylic and L_{oil} of oil, the combined transmission at wavelength λ factorizes as follows:

$$T_{\mathrm{tot}}(\lambda) = \exp\big[-L_{\mathrm{acrylic}}/\lambda_{\mathrm{abs}}^{\mathrm{acrylic}}(\lambda)\big] \times \exp\big[-L_{\mathrm{oil}}/\lambda_{\mathrm{abs}}^{\mathrm{oil}}(\lambda)\big]. \tag{8.2}$$

Parametric scans over $L_{\mathrm{acrylic}} \in [5, 30]\,\mathrm{cm}$ and $L_{\mathrm{oil}} \in [0.5, 1.5]\,\mathrm{m}$ produce a two-dimensional transmission map Fig.8.2) that highlights the region of highest photon survival efficiency. This spherical-shell study decouples shape effects from pure thickness dependence, enabling straightforward translation of the optimal layer depths into any final detector form factor without altering the optical performance.

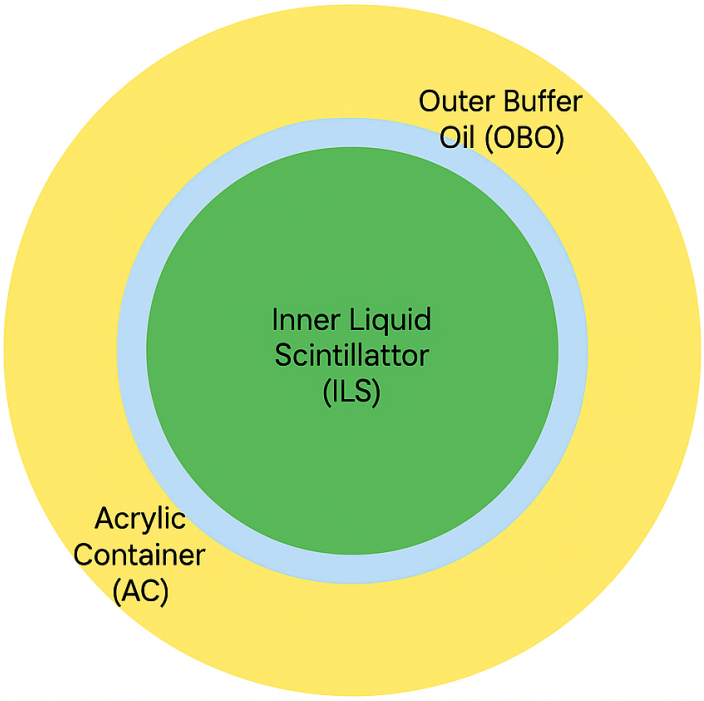

Figure 8.1: Idealized shell model of detector for parametric layer-thickness geometry

8.3 Optical Properties

In all ray-tracing studies, the wavelength-dependent optical parameters of each detector medium were drawn from the most recent laboratory characterizations and benchmarked against validated Geant4 optical simulations. The liquid scintillator (LS) was modeled on a LAB base with PPO fluor(3.5g/L), using an emission spectrum measured under cold-water conditions. Its refractive index and absorption length were parameterized as smooth, empirically derived functions of wavelength.

The acrylic containment vessel was assigned optical properties consistent with UV-grade cast acrylic, based on published literature values, given their widespread availability in manufacturer datasheets. Both its refractive index dispersion and attenuation length were treated as continuous functions of wavelength, reflecting the high transparency of the material across the scintillation band.

The buffer oil was represented by a mineral-oil blend whose refractive index dispersion and absorption profile were similarly parameterized from transmission data, ensuring that the simulated oil layer reproduced the wavelength-dependent loss characteristics seen in lab measurements.

All internal boundaries (LS–acrylic, acrylic–oil, oil–vacuum) were implemented as dielectric–dielectric interfaces using the Geant4 "glisur" surface model. Fresnel reflections were computed from the wavelength-dependent refractive indices, and a small, wavelength-independent surface roughness was applied to each interface to account for microscopic surface imperfections.

8.4 Ray Tracing Simulation Framework

A custom photon-tracing framework was developed in Python and Geant4 to simulate optical photon propagation. Each simulation run generates a large ensemble of photons emitted isotropically from within the LS volume. Photon wavelengths are sampled according to the PPO emission spectrum. As each photon travels through LS, acrylic, and BO layers, it is subjected to:

- Absorption based on absorption lengths $\lambda_{\text{abs}}(\lambda)$
- Refraction at interfaces via Snell's Law
- Fresnel reflection losses at boundaries

Transmission efficiency is defined as the fraction of photons that survive all layers and reach the outer boundary of buffer oil without being absorbed. The simulation is repeated across a grid of acrylic and buffer oil thicknesses to generate a 2D map of transmission performance.

8.5 Results and Analysis

8.5.1 Overall Transmission Trends

The total transmission efficiency was found to decrease with increasing thickness of both acrylic and buffer oil. This behavior follows from the exponential attenuation governed by the Beer–Lambert law:

$$T(L, \lambda) = \exp\left(-\frac{L}{\lambda_{\text{abs}}(\lambda)}\right) \tag{8.3}$$

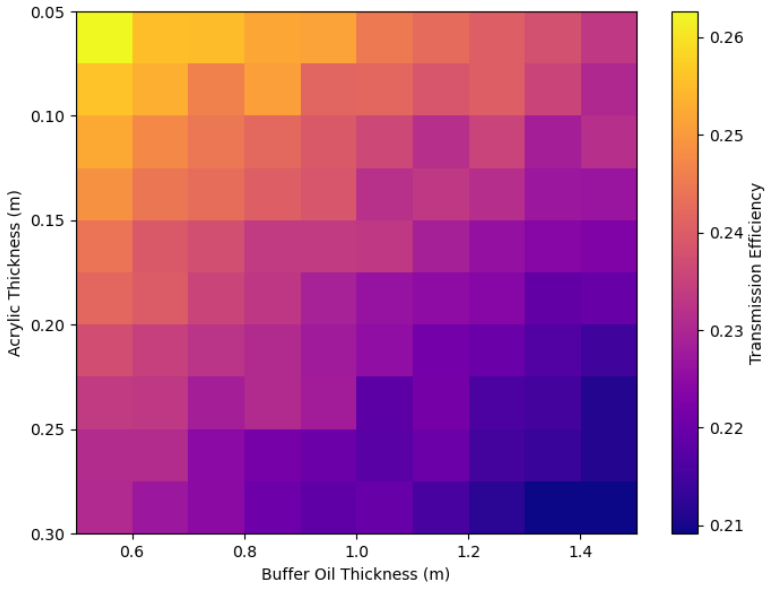

Figure 8.2: Overall transmission trends with varying acrylic and buffer oil thickness

This attenuation is more severe for shorter wavelengths due to stronger absorption. In all tested geometries, the highest transmission was observed when both the acrylic and buffer oil layers were kept thin. As the optical path through each medium increases, the probability of photon loss through absorption rises exponentially.

8.5.2 Wavelength-Resolved Efficiency

To disentangle the spectral effects, the transmission simulation was repeated across four wavelength bins: 350-370 nm, 370-400 nm, 400-430 nm, and 430-500 nm. Heatmaps show that:

- The 350-370 nm range is heavily absorbed in both LS and acrylic, yielding the lowest transmission.
- The 370-400 nm range shows improved transmission but is still limited by absorption.
- The 400-430 nm band exhibits the best balance between high emission intensity and moderate absorption lengths.
- The 430-500 nm range has the best raw transmission efficiency due to long absorption lengths, but contributes less overall because the emission spectrum is weaker in this range.

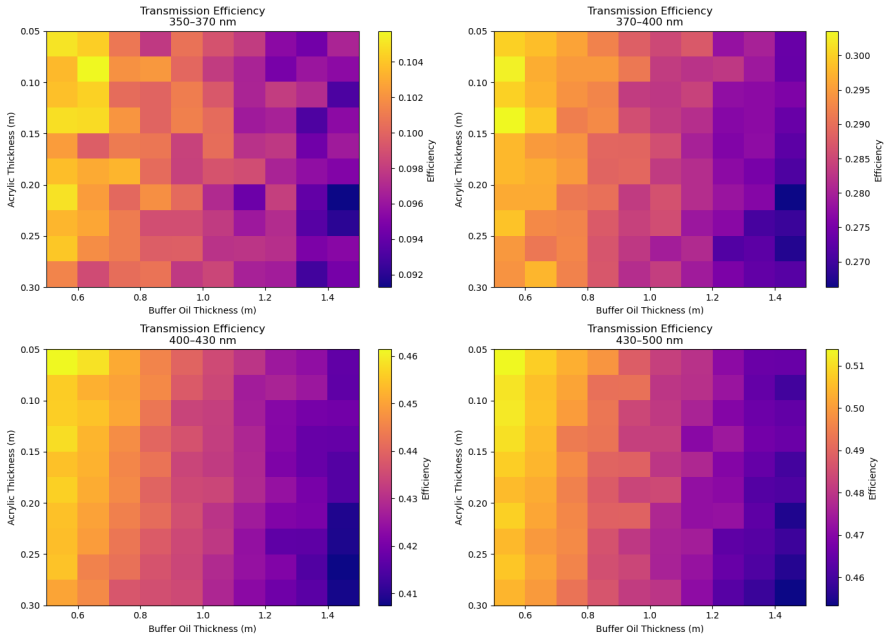

Figure 8.3: Transmission efficiency maps for different wavelength bins. Each map shows how efficiency varies with acrylic and buffer oil thicknesses.

To determine which wavelength region contributes the most to total detected light, the product of transmission efficiency and relative emission intensity for each bin was computed. The resulting plot confirms that the 400-430 nm band dominates total contribution to transmission due to its peak in both emission spectrum and favorable optical properties.

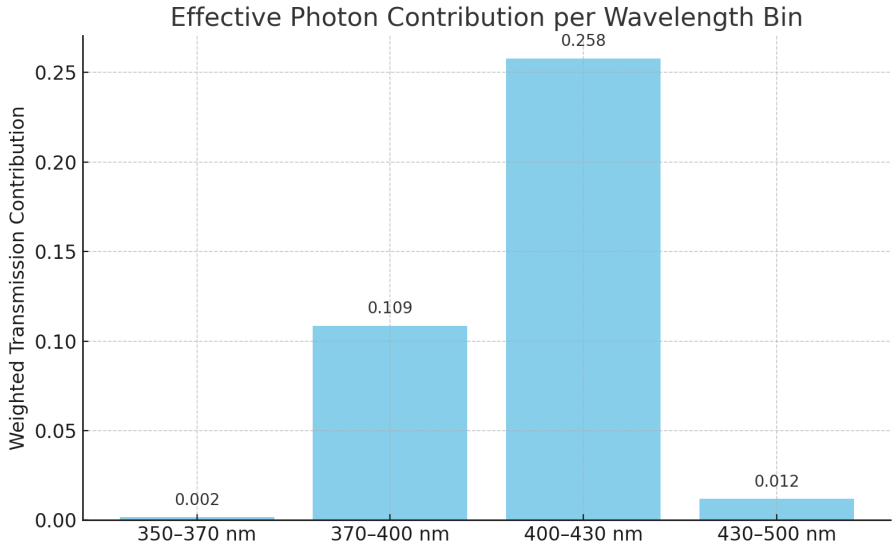

Figure 8.4: Weighted transmission contribution by wavelength bin, combining both emission probability and transmission efficiency.

8.6 Discussion

These findings confirm that detector optical performance is tightly linked to both geometry and wavelength-dependent material properties. While thin acrylic and buffer oil layers are desirable for maximizing light yield, practical design must also consider mechanical stresses, radiopurity, and chemical compatibility. Additional studies involving finite element analysis and mechanical stress tolerances are required to

identify feasible designs.

8.7 Conclusion

A detailed optical ray tracing study was performed for a large-scale liquid scintillator detector to optimize photon transmission efficiency. Wavelength-dependent material properties were used to simulate realistic light propagation. The study concludes that thinner acrylic and buffer oil layers yield better transmission, particularly in the dominant scintillation emission band. This analysis sets the stage for integrated optimization studies that combine optical, structural, and cost considerations. The results demonstrate that the detector's optical design must carefully weigh thickness constraints of the acrylic and buffer oil layers.

Chapter 9

Conclusion and Future Prospects

9.1 Conclusion

This study presents a comprehensive simulation-driven assessment of a deep-sea prototype liquid scintillator detector, with the broader objective of informing the design of a future large-scale ocean-based neutrino observatory. Detailed `Geant4` simulations were conducted to evaluate the optical performance and intrinsic resolution of the prototype module, incorporating environmental effects and improved detector geometry. The simulations showed that operation in the marine environment — with lower temperatures and optimized optical modules can yield a photoelectron signal enhancement of approximately 79%, translating to an intrinsic resolution of about $13.3/\sqrt{E}$.

A critical aspect of this work was the assessment of environmental and intrinsic background radiation sources such as ^{238}U, ^{232}Th, ^{40}K, and ^{60}Co present in seawater, sediments, and detector materials. Simulations showed that these sources contribute minimally to the detector response when compared to standard calibration sources like ^{137}Cs, thus validating the stability of the detector's energy response in realistic deep-sea conditions.

Moreover, preliminary optical design studies for a kiloton-scale detector geometry were conducted using custom ray-tracing simulations. These studies evaluated the impact of varying the thicknesses of the acrylic and buffer oil layers on scintillation photon transmission. The results demonstrated that thinner layers (5–12 cm for acrylic and 0.5–0.8 m for buffer oil) yield significantly improved light transmission, particularly in the 400–430 nm wavelength band where both emission intensity and transmission are optimal. This finding serves as a key design guideline for scaling up to a full-scale ocean-bottom detector.

9.2 Future Prospects

Long-term Deployment and Validation

The prototype's upcoming deployment at JAMSTEC's deep-sea observatory will provide critical empirical validation of the simulation framework. Long-duration operation will test the durability and stability of the detector's components under marine conditions. The established background baseline will also enable performance monitoring and anomaly detection in post-deployment data.

Technological development

Future improvements in low-power electronics, autonomous control systems, alarm systems and pressure-resistant sensor modules will be critical for large scale, long-term deployment in remote oceanic locations.

Advanced Optical Design for Large-Scale Detectors

The ray-tracing simulations highlight early optimization strategies for large detector designs. Future work should integrate mechanical and radiopurity constraints with the optical findings to refine material choices and layer thicknesses. Additionally, improvements in optical modeling, including the use of reflectors or wavelength-shifting devices — could further enhance light collection efficiency.

Integration of Optical and Structural Simulations

A critical next step is the integration of the optical simulation framework with finite-element mechanical simulations. This would ensure that the optimized geometry is also structurally feasible under high-pressure deep-sea conditions, especially accounting for stress tolerance in the acrylic and stainless steel layers.

Toward a Modular, Scalable Observatory

The findings from both the prototype and the large-scale simulation studies lay the foundation for a modular, scalable system capable of precision geoneutrino measurements. The ability to optimize optical and background performance at the module level enables the possibility of a distributed ocean-bottom array, capable of global geoneutrino flux mapping and contributing significantly to both neutrino physics and Earth sciences.

In conclusion, this prototype serves as a critical first step toward realizing a full-scale ocean-based neutrino observatory. Its successful operation under deep-sea conditions lays the initial groundwork for future detectors that could transform both neutrino science and our understanding of Earth's interior.

Bibliography

[1] C. L. Cowan et al. "Detection of the Free Neutrino: a Confirmation". In: *Science* 124 (3212 1956), pp. 103–104. DOI: 10.1126/science.124.3212.103.

[2] A. Gando et al. "Constraints on θ_{13} from a three-flavor oscillation analysis of reactor antineutrinos at KamLAND". In: *Phys. Rev. D* 83 (5 2011), p. 052002. DOI: 10.1103/PhysRevD.83.052002.

[3] L. Wolfenstein. "Neutrino oscillations in matter". In: *Phys. Rev. D* 17 (9 May 1978), pp. 2369–2374. DOI: 10.1103/PhysRevD.17.2369. URL: https://link.aps.org/doi/10.1103/PhysRevD.17.2369.

[4] S. P. Mikheyev and A. Yu. Smirnov. "Resonant Neutrino Oscillations in Matter". In: *Progress in Particle and Nuclear Physics* 23 (1989), pp. 41–136. DOI: 10.1016/0146-6410(89)90008-2.

[5] C. Jaupart, S. Labrosse, and J.-C. Mareschal. "7.06 - Temperatures, Heat and Energy in the Mantle of the Earth". In: *Treatise on Geophysics*. Ed. by Gerald Schubert. Amsterdam: Elsevier, 2007, pp. 253–303. ISBN: 978-0-444-52748-6. DOI: https://doi.org/10.1016/B978-044452748-6.00114-0. URL: https://www.sciencedirect.com/science/article/pii/B9780444527486001140.

[6] William Thomson. "XV.— On the Secular Cooling of the Earth". In: *Transactions of the Royal Society of Edinburgh* 23.1 (1862), pp. 157–169. DOI: 10.1017/S0080456800018512.

[7] L. M. Krauss, S. L. Glashow, and D. N. Schramm. "Antineutrino astronomy and geophysics". In: *Nature* (1984). DOI: 10.1038/310191a0.

[8] T. Araki et al. "Experimental investigation of geologically produced antineutrinos with KamLAND". In: *Nature* (2005). DOI: 10.1038/nature03980.

[9] G. Bellini et al. "Observation of geo-neutrinos". In: *Phys. Lett. B* 687 (4 2010), pp. 299–304. DOI: 10.1016/j.physletb.2010.03.051.

[10] S. Abe et al. "Abundances of Uranium and Thorium Elements in Earth Estimated by Geoneutrino Spectroscopy". In: *Geophys. Res. Lett.* (2022). DOI: 10.1029/2022GL099566.

[11] M. Agostini et al. "Comprehensive geoneutrino analysis with Borexino". In: *Phys. Rev. D* 101 (1 2020), p. 012009. DOI: 10.1103/PhysRevD.101.012009.

[12] L. G. Sammon and W. F. McDonough. "Quantifying Earth's radiogenic heat budget". In: *Earth Planet. Sci. Lett.* 593 (2022), p. 117684. DOI: 10.1016/j.epsl.2022.117684. URL: https://www.sciencedirect.com/science/article/pii/S0012821X2200320X.

[13] R. S. Raghavan et al. "Measuring the Global Radioactivity in the Earth by Multidetector Antineutrino Spectroscopy". In: *Phys. Rev. Lett.* 80 (3 1998), pp. 635–638. DOI: 10.1103/PhysRevLett.80.635.

[14] W. F. McDonough and H. Watanabe. "Neutrino Geoscience: Review, Survey, Future Prospects". In: *Core-Mantle Co-Evolution*. American Geophysical Union (AGU), 2023. Chap. 1, pp. 1–16. DOI: 10.1002/9781119526919.ch1.

[15] O. Šrámek et al. "Geophysical and geochemical constraints on geoneutrino fluxes from Earth's mantle". In: *Earth Planet. Sci. Lett.* 361 (2013), pp. 356–366. DOI: 10.1016/j.epsl.2012.11.001.

[16] E. Garnero and C. Richardson. "The mysterious, massive structures in Earth's deep mantle". In: *Phys. Today* 77.12 (2024), pp. 36–43. DOI: 10.1063/pt.mzrx.ddag.

[17] T. Kasaya et al. “Multidisciplinary observations at an expandable sub-marine cabled station off the Hatsushima Island, the Sagami Bay, Japan”. In: *2007 Symposium on Underwater Technology and Workshop on Scientific Use of Submarine Cables and Related Technologies*. 2007, pp. 674–676. DOI: 10.1109/UT.2007.370819.

[18] R. Iwase et al. “Off Hatsushima Island observatory in Sagami Bay: multidisciplinary long term observation at cold seepage site with underwater mateable connectors for future use”. In: *2003 International Conference on Physics and Control (Cat. No. 03EX708)*. 2003, pp. 31–34. DOI: 10.1109/SSC.2003.1224105.

[19] Hiroyasu Momma et al. “Preliminary results of a three-year continuous observation by a deep seafloor observatory in Sagami Bay, central Japan”. In: *Physics of the Earth and Planetary Interiors* 108.4 (1998), pp. 263–274. ISSN: 0031-9201. DOI: 10.1016/S0031-9201(98)00107-1. URL: https://www.sciencedirect.com/science/article/pii/S0031920198001071.

[20] Masao Nakanishi, Hiromi Fujimoto, and Hideyuki Murakami. “Temperature Variations in the Calyptogena Community off Hatsushima Island, Sagami Bay”. In: *Zisin (Journal of the Seismological Society of Japan. 2nd ser.)* 48.1 (1995-1996). Released on J-STAGE March 11, 2010, pp. 71–79. ISSN: 0037-1114. DOI: 10.4294/zisin1948.48.1_71. URL: https://www.jstage.jst.go.jp/article/zisin1948/48/1/48_1_71/_article/-char/en.

[21] Taichi Sakai. “Development of detector components for low-temperature and high-pressure environment, and performance evaluation with simulation toward ocean bottom anti-neutrino detector OBD”. Unpublished. MA thesis. Tohoku University, 2022.

[22] R. Abbasi et al. “D-Egg: A dual PMT optical module for IceCube”. In: *J. Instrum.* 18.04 (2023), P04014. DOI: 10.1088/1748-0221/18/04/P04014.

[23] Takumi Araki. “Development study of a small prototype detector toward realization of ocean bottom neutrino detector OBD”. Unpublished. MA thesis. Tohoku University, 2025.

[24] T. Kasaya et al. “Trial of Multidisciplinary Observation at an Expandable Sub-Marine Cabled Station “Off-Hatsushima Island Observatory” in Sagami Bay, Japan”. In: *Sensors* 9 (11 2009), pp. 9241–9254. DOI: 10.3390/s91109241.

[25] Glenn F Knoll. *Radiation detection and measurement; 4th ed.* New York, NY: Wiley, 2010. URL: https://cds.cern.ch/record/1300754.

[26] S. Agostinelli et al. “Geant4—a simulation toolkit”. In: *Nucl. Instrum. Methods Phys. Res. A* 506 (3 2003), pp. 250–303. DOI: 10.1016/S0168-9002(03)01368-8.

[27] H. H. Veeh. “Deposition of uranium from the ocean”. In: *Earth Planet. Sci. Lett.* 3 (1967), pp. 145–150. DOI: 10.1016/0012-821X(67)90026-X.

[28] N. Khaustova et al. “The Study of Uranium Accumulation in Marine Bottom Sediments: Effect of Redox Conditions at the Time of Sedimentation”. In: *Geosciences* 11 (8 2021), p. 332. DOI: 10.3390/geosciences11080332.

[29] H. Takahashi et al. “Reconstructing the chronology of the natural and anthropogenic uranium isotopic signals in a marine sediment core from Beppu Bay, Japan”. In: *Heliyon* 9 (4 2023), e14153. DOI: 10.1016/j.heliyon.2023.e14153.

[30] C. T. Hayes. “Timekeepers for Trace Elements in the Global Ocean: The Thorium Stopwatches”. In: *Oceanography* 37 (2 2024). DOI: 10.5670/oceanog.2024.412.

[31] D. Heye. “Uranium, thorium, and radium in ocean water and deep-sea sediments”. In: *Earth Planet. Sci. Lett.* 6 (2 1969), pp. 112–116. DOI: 10.1016/0012-821X(69)90128-9.

[32] J. G. Ryan and C. Chauvel. “The Subduction-Zone Filter and the Impact of Recycled Materials on the Evolution of the Mantle”. In: *Treatise on Geochemistry*. Ed. by H. D. Holland and K. K. Turekian. 2nd. Vol. 3.13. Oxford: Elsevier, 2014, pp. 479–508. DOI: 10.1016/B978-0-08-095975-7.00211-4.

[33] F. Culkin and R. A. Cox. “Sodium, potassium, magnesium, calcium and strontium in sea water”. In: *Deep Sea Res. Oceanogr. Abstr.* 13 (5 1966), pp. 789–804. DOI: 10.1016/0011-7471(76)90905-0.

[34] W. Maneschg et al. “Measurements of extremely low radioactivity levels in stainless steel for GERDA”. In: *Nucl. Instrum. Methods Phys. Res. A* 593.3 (2008), pp. 448–453. DOI: 10.1016/j.nima.2008.05.036.